DELIVERABLE REPORT

Deliverable no. / title:	4.3 / Upscaling of symmetric unit cell electrode model
Lead beneficiary:	ZHAW - Institute of Computational Physics
Nature of deliverable:	Report
Dissemination level:	Public
Due date:	M36 / December 2022

Grant Agreement number:	**875489**
Project acronym:	**SONAR**
Project title:	**Modelling for the search for new active materials for redox flow batteries**
Funding scheme:	**H2020-LC-BAT-2019**
Coordinator:	Fraunhofer ICT Jens Noack **Tel:** 0049 721 4640 870 **E-mail:** jens.noack@ict.fraunhofer.de
Project website:	www.sonar-redox.eu
Disclaimer:	This project has received funding from the European Union's Horizon 2020 research and innovation programme under Grant Agreement no. 875489. This report reflects only the authors' view. The funding agency is not responsible for any use made of the information it contains.

Table of contents

1 Introduction

Porous electrodes (PEs) are ubiquitous in industrial electrochemistry, as they allow for the application of high electric currents, while maintaining a compact size of the electrochemical reactor. In recent years, one particularly interesting application of PE for novel large-scale

energy storage devices, referred to as (redox) flow batteries (FB), gained popularity. Such industrial-scale systems, although being still an emerging technology, constitute one of the most promising solutions to the electric grid instability, caused by a rapidly expanding share of intermittent renewable energy resources [37, 57]. Flow battery technology is one of the main candidates for storing large amounts of electric energy on sites, where the construction of established grid-imbalance equalizing solutions, such as pumped-hydro storage, is not feasible.

The flow distribution inside the porous structures plays an important role for the overall performance of FB systems. In FBs, the electrochemical reactions occur at the surface of a porous medium. The dissolved electro-active species are transported in the electrolyte by means of forced convection, diffusion, and migration. In general, all of these phenomena are strongly coupled and highly non-linear, which largely complicates the theoretical description of FB operation [52].

To accurately simulate a FB cell the coupled transport processes at the pore-scale must be considered. However, the simulation of an entire macroscopic cell using a fully resolved pore-scale description would require prohibitively large computational resources even for modern computer clusters. Instead, efficient macroscopic models are typically used for cell-scale simulations. For such macroscopic models to accurately reflect the sub grid pore-scale processes it must be ensured that all relevant information is retained when increasing the model abstraction through an upscaling process [52].

In this work we investigate the application of the volume-averaging method (VAM) to describe and simulate the macroscopic mass transport of the electro-active species, driven by convection, diffusion, and a Butler-Volmer (BV) type heterogeneous reaction at the electrode surfaces. Here we consider simplified, periodic PE geometries at the pore-scale with a focus on elucidating the effect of the pore-scale geometry on macroscopic transport properties. After presenting verification studies against published results, we discuss the determined effective properties, such as the dispersion and effective reaction rate. We highlight modelling errors that result from often-used oversimplified analytical solutions in cell-scale FB models. Finally, we present the application of the effective material properties to the transport through a macroscopic electrode.

2 Porous Electrodes for Flow Battery Applications

One of the main factors hindering the ubiquitous spread of FB technology on the market is high cost. Thus, to lower the levelised cost of storage (LCOS), it is highly desired to design more robust FB systems with superior characteristics, such as competitive round-trip efficiency and long battery lifetime.

Optimisation of FB electrodes is one of the core ideas towards improving the battery per-

formance. Focusing on PEs only, two main performance enhancement methods can be distinguished [16]: On the one hand, the electrode surface may be functionalised with deposited nanomaterials (e.g. carbon nanorods) or by thermal pre-treatment. The fibre precursor itself may also be changed, producing fibre characteristics dissimilar to that in commercial materials. On the other hand, the morphology of the PE can be varied, such that desired structural features appear in a cascade of length scales. In this study, we turn our attention to computationally analyze the latter idea.

Engineered pore structures can help to approach the ideal electrolyte transport process: convection to meso-scale pores through micro-scale pores, then diffusion into nanoscale pores and heterogeneous reaction [5, 46]. Such gradient-pore oriented graphite felt, manufactured with pore sizes spanning from nano to micro-scales, has demonstrated energy efficiency improvements of a vanadium flow battery (VFB) by nearly 20 %, compared to pristine graphite felt electrodes [46]. Novel materials with gradients of porosity within their volumes were found to be capable of delivering 69 % higher discharge capacity than these with conventional VFB electrode design [24].

FB systems commonly employ carbon-based porous material consisting of micrometre-thickness fibres synthetised from precursors such as polyacrylonitrile. Carbon materials are relatively cheap, highly conductive, and chemically stable in corrosive electrolyte solutions. PEs utilised in modern FB have been historically derived from proton-exchange membrane fuel cells (PEMFCs) gas diffusion layer materials, which were, however, not designed to perform optimally in FB applications [15]. Hence, a high potential for further refinements exists, for example via computer simulation-aided PE architecture design.

Key Metrics of Porous Electrodes Porous materials, whether natural or synthesised, are characterised by a complicated morphology of the solid material and the complementary void volume, through which the electrolyte flows. The geometry, connectivity and orientation (topology) of these domains are typically disordered. Thus, these porous domains can be analysed in terms of statistical descriptions.

The most fundamental geometric property of a porous electrode is the porosity $\varepsilon \in (0,1)$, which is the ratio of the void volume to the total volume of the porous material. The total geometric surface area of the void-matrix interface divided by the total volume which encloses this surface is referred to as specific surface area, a_v $(\mathrm{m}^2\,\mathrm{m}^{-3})$. However, the surface area available for redox reactions can be different from the geometrical surface area e.g., due to steric effects of the molecules. Tortuosity, τ, is another often-used parameter, describes the length of the effective path of transport (of mass, charge, heat, etc.) across the PE divided by the geometric distance.

Porosity, tortuosity and specific surface are, as expected, correlated [10]. In macroscopic

electrode models, the tortuosity factor is often defined as [42]

$$D^{\text{eff}} = D\frac{\varepsilon}{\tau}, \tag{1}$$

where D denotes the molecular diffusivity and D^{eff} is the effective diffusivity at the macroscale, which is affected by the pore-scale morphology and transport processes. The well-known Bruggeman relation for random porous media used for more than 50 years is given by

$$\tau = \varepsilon^{-1/n}, \tag{2}$$

where $n = 1$ for porous materials with randomly embedded cylinders and $n = 2$ for spheres, see [42]. Thanks to its simplicity, the Bruggeman relation has been used extensively in FB modelling literature (cf. e.g. [29, 35, 55]).

Despite the abundant usage of the Bruggeman approach in the porous electrode modelling literature, experimental studies on Li-ion batteries indicate great deviations of tortuosity values predicted by Eq. (2) from measured data due to the complexity of the porous structures [10]. There are numerous reasons for this discrepancy. First, real PEs are characterised by a range of tortuosities, rather than a single, average value. Moreover, microstructural variations can locally increase the tortuosity by a factor of three [26]. Other explanations are sought in randomness in particle (solid matrix) packing and local inhomogeneities. The Bruggeman relation was originally derived assuming spherical and cylindrical obstruction to transport [42], whereas porous electrodes in FB consist of oblong fibres, which casts further doubts on the applicability of this relation for FB modelling. To date, no good correlation between microstructure and macroscopic tortuosity has been found [10].

Incorporating meso- and micro-scale effects into component, stack and cell-types of models is vital not only for increasing model predictability, but also for improving the understanding of processes occurring within PEs [28]. Current techniques allow for manufacturing PE with well-controlled micro- and nanostructure features. The remaining question persists: what is the optimal pore architecture to maximize electrode power efficiency [28]?

2.1 Established Methods for Simulating Porous Electrodes

Continuum Models with Simplified Closure Relations In the most typical FB modelling approach, momentum, mass, heat and charge conservation equations are resolved in one to three spatial dimensions to virtually represent different parts of the flow cell or stack. The balanced quantities are treated as a macroscopic continuum (Newman-type [34] models), meaning that the governing equations are written for averaged (over the representative elementary volume, REV) quantities, rather than for their intrinsic (intra-pore) counterparts [9, 14]. In this approach,

physical micro-properties, such as porosity and tortuosity, are spatially uniform. Transport properties (such as the diffusion coefficient or electrical conductivity) in the constitutive relations need to be corrected for the fact that the considered balanced quantities in liquid solution or gas phase (e.g. concentration) are in fact averaged over a domain consisting of both electronically conductive solid electrode phase (the so-called matrix) and void phase (taken by the liquid electrolyte or gas). However, such corrections are not particularly rigorous and only aim to better approximate the empirical data. Solving a true mathematical closure problem is accomplished in the up-scaling process which we describe in section 2.2.

There are numerous examples of macroscopic continuum modelling approaches based on (over-)simplified relations in the literature of FB modelling, available for a variety of FB systems. For example, Zhang et al. [57] simulated a VFB cell in 2D using the Brinkman equation for electrolyte flow with the Kozeny-Carman relation to estimate hydraulic permeability of the electrode, and the Bruggeman relation for diffusion coefficient and electronic conductivity. Albeit so common, such simple corrections of the intrinsic transport properties should be critically assessed, and the underlying assumptions verified for particular PE structures [9, 25]. It is commonplace that microstructure parameters, such as porosity or specific surface area remain fitting parameters at the macroscopic level to better match model results with macroscopic observables (e.g. polarisation curves) [18]. Evidently, such an approach may jeopardise the predictive power of macroscopic continuum model simulations.

2.2 Up-scaling Methods

When dealing with the disparity of physical length scales in PEs, trade-offs must be sought to allow for obtaining accurate results at affordable computational costs. “Brute-force” modelling of the whole PE volumes (e.g., hundreds of cm^2) used in industrial FBs to resolve micrometre pores is impractical (or even impossible), due to prohibitively long computation times. On the other hand, simulating FB electrodes using the computationally efficient macrohomogeneous approach requires additional subgrid-scale models to capture the electrode morphology effects on cell performance.

Mathematical upscaling methods can be used to rigorously determine the effective parameters in macroscopic transport equations, which reflect the effect of the pore-scale processes [11, 38]. Various up-scaling methods exist and have been applied in numerous fields of science. All methods, however, share two common goals: (1) deriving macroscopic balance laws and (2) formulating closure problems for transport parameters to be used in the balance laws. In fact, many macroscopic models were first devised from empirical observations (e.g. Darcy’s law, Brinkman equation) and only later derived using the formal mathematical upscaling [4].

In this work, we select the VAM to extend the currently available literature studies of systems with porous structures, in which flow phenomena, together with chemical reactions (heterogeneous or homogeneous), occur by including the electrochemical reaction interface (of BV-type) in the PE model. We focus particularly on the modelling of FBs, albeit the procedures discussed herein can be applied to other electrochemical flow cells, such as electrolysers.

The VAM is used to derive spatially homogeneous representations of conservation laws in porous media. Processes in these media usually occur over various length scales, and the information from the smaller scale is systematically conveyed to the larger scale in the volume averaging process. This up-scaling procedure has been well documented in the literature [43, 49, 50] and applied in a variety of fields, for instance chemical engineering [19] or groundwater hydrology [36].

Literature studies on the VAM most relevant for the application to FBs, concern up-scaling of inertial and creeping flow in porous media [2], dispersion of mass [45], advection-diffusion-reaction equations (heterogeneous and homogeneous, zeroth and first order reactions) [43, 44], and non-linear reactions: homogeneous [31] and heterogeneous [20].

In the matter of electrochemistry, Le et al. [28] developed an up-scaled PE model of a chronoamperometric experiment, in which electron transfer was described using the BV equation and the mass transport at the pore-scale was assumed to be dominated by Fickian diffusion. Ultimately, however, the non-linear BV equation employed as the boundary condition in this study was simplified to a linear Tafel-like equation. For a given sufficiently high and constant overpotential, the surface reaction term was thus reduced to a first-order reaction. The authors used the VAM to derive effective parameters in representative, periodic PE consisting of spheres in simple cubic (SC), body-centered cubic (BCC) and face-centered cubic (FCC) geometric arrangements. The effective parameters resulting from the VAM were employed in a simplified 1D geometry to simulate the transient chronoamperometric response. The VAM results were then compared with a direct numerical simulation (DNS) of the same electrode structures and the agreement was excellent. Le et al. achieved roughly 3100 speed-up of the 1-D upscaled model compared to the DNS approach.

3 Modelling of Porous Electrodes

Transport phenomena within PEs are inherently of a multiscale nature, as depicted in Fig. 1, where a hierarchy of scales is exhibited, starting from the macroscale in panel (A), over the mesostructure (B), the microstructure (C), to the surface phenomena (D).

We are interested in macroscopic transport models for PEs, which allow for the efficient simulation of large electrode domains with a characteristic length scale L. On the other hand, the pore-scale structure has a characteristic length scale l, which is assumed to be much

smaller compared to the macroscopic scale. By means of the VAM the effects of the pore-scale morphology and transport are incorporated into the macroscopic description.

3.1 Pore-scale Transport Modelling

The electrode geometry is assumed to be rigid and spatially periodic, so that the electrode material is generated by translational copies of a periodic unit cell. In Fig. 1 A) we show an exemplary periodic porous electrode structure generated by a simple unit cell geometry displayed in Fig. 1 B). The unit cell domain is partitioned into an electrode domain V_σ and electrolyte domain V_β, separated by an interface domain $A_{\beta\sigma}$.

At the pore-scale we assume the flow velocity to be small enough for inertial effects to be negligible. Furthermore, we assume dilute concentrations of the electro-active species. Assuming a Newtonian fluid, the convective flow can be described in terms of the Stokes equation

$$\nabla p - \nabla^2 \mathbf{v} = 0, \quad \nabla \cdot \mathbf{v} = 0, \quad \mathbf{r} \in V_\beta \tag{3}$$

with no-slip boundary condition on the electrode surface.

To simplify the governing equations we assume the electronic resistivity to be negligible both within the electrode material and the electrolyte phase. In practice the latter condition can be realized experimentally by the usage of a supporting electrolyte. In this work we assume isothermal conditions and set the constant temperature to $T = 298.15$ K. Additionally, we assume the average separation of the pore-scale electrode structures to be much larger compared to the Debye length, which allows to impose the electroneutrality condition within the electrolyte phase. These simplifications allow the mass transport of the electroactive species i to be described in terms of an advection-diffusion equation

$$\mathbf{v} \cdot \nabla c_i = D \nabla^2 c_i, \quad \mathbf{r} \in V_\beta, \tag{4}$$

where D denotes a diffusion coefficient, which is assumed to be constant and equal for all electro-active species. The coupling to the heterogeneous reactions at the electrode-electrolyte interface can be stated generally as

$$-D \nabla c_i \cdot \mathbf{n}_{\beta\sigma} = r_i(c_1, \ldots, c_N), \quad \mathbf{r} \in A_{\beta\sigma}, \tag{5}$$

where $\mathbf{n}_{\beta\sigma}$ is the unit vector pointing from the electrolyte into the solid electrode phase (see Fig. 2) and r_i denotes a general production term due to the electrochemical reaction.

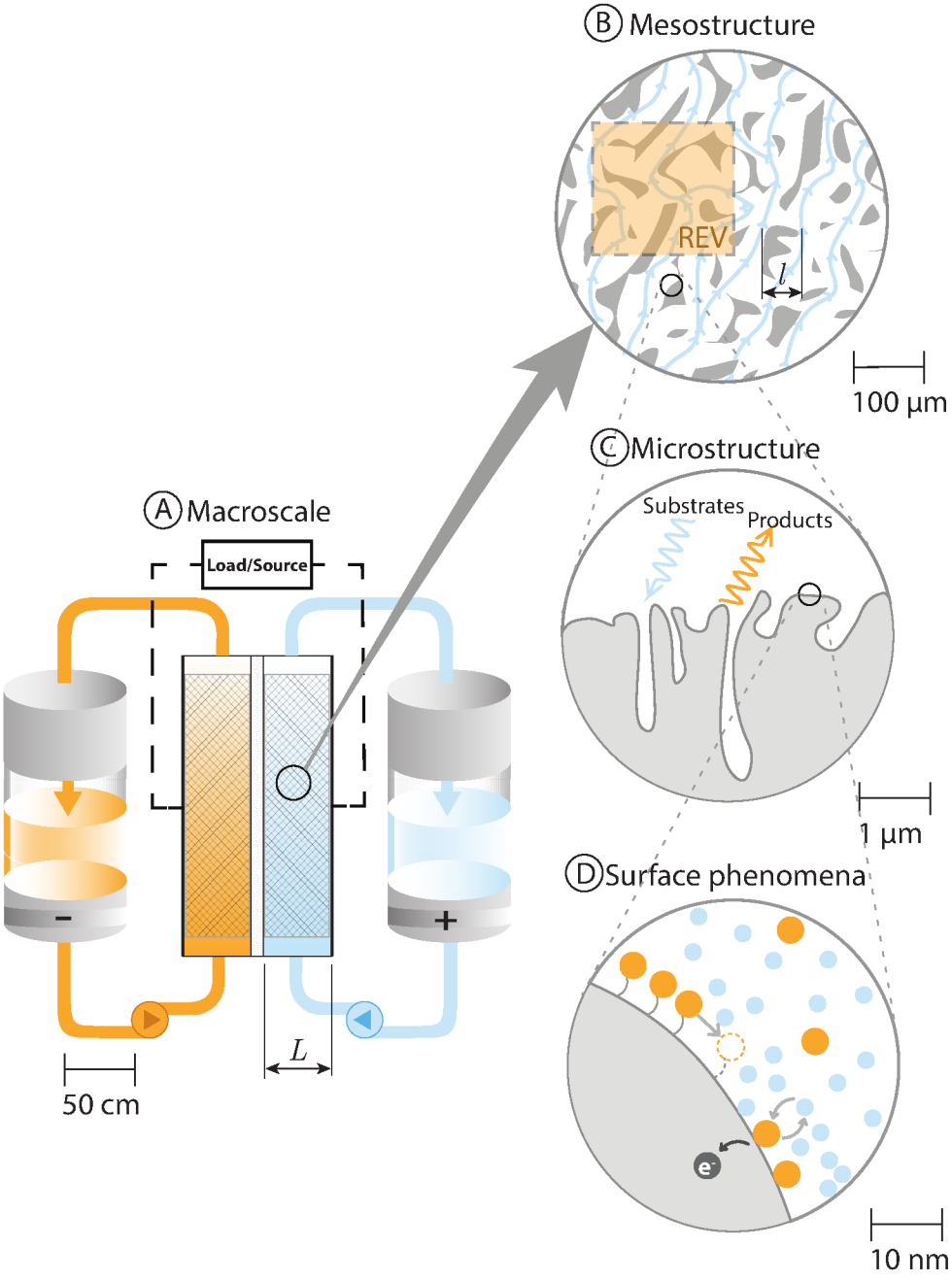

Figure 1: The cascade of length scales involved in FB models: A) Macro-scale featuring the characteristic macroscopic length scale L; B) Meso-scale structure with characteristic pore-scale length l over a representative elementary volume (REV); C) Micro-pore scale, where the dominant transport mode is molecular diffusion and migration in the electric field; D) Surface phenomena on the atomistic scale.

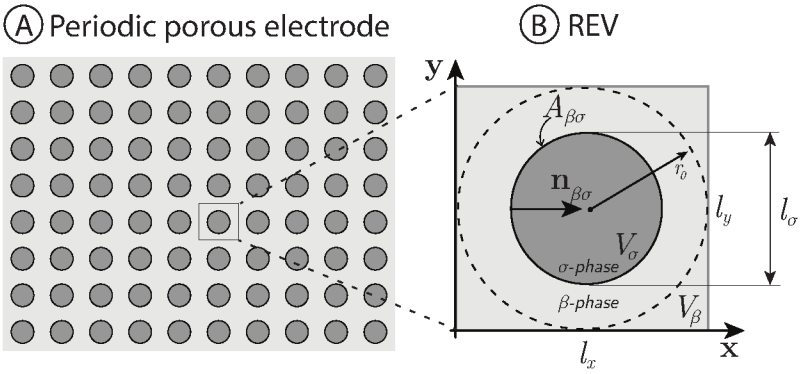

Figure 2: A) Macroscopic representation of a simplified porous electrode - a periodic medium composed of conductive fibres, B) the corresponding representative elementary volume

3.1.1 Electrochemical Reactions

In the electrochemical context of this work, we consider the reversible one-electron transfer redox reaction

$$\mathrm{Ox} + \mathrm{e} \rightleftharpoons \mathrm{Red}. \tag{6}$$

We model the kinetics of Reaction 6 using the *practical* form [12] of the Butler-Volmer equation

$$j = \frac{j_{0,\mathrm{ref}}}{c_{\mathrm{ref}}} \left(e^{(1-\alpha) f \eta_{\mathrm{ref}}} c_{\mathrm{red}} - e^{-\alpha f \eta_{\mathrm{ref}}} c_{\mathrm{ox}} \right), \tag{7}$$

where j is the current density at the electrode surface ($\mathrm{A\,m^{-2}}$), c_{ref} denotes a fixed reference concentration ($\mathrm{mol\,m^{-3}}$), α is the transfer coefficient, and

$$j_{0,\mathrm{ref}} = F k c_{\mathrm{ref}}, \quad \eta_{\mathrm{ref}} = E - E_{\mathrm{eq}}(c_{\mathrm{ref}}), \quad f = \frac{F}{RT}, \tag{8}$$

are the reference exchange current density, the overpotential with respect to a reference state, and the inverse thermal voltage ($\mathrm{V^{-1}}$). In Eq. (8), k denotes the heterogeneous reaction rate constant ($\mathrm{m\,s^{-1}}$), E is the electrode polarization (V), and E_{eq} is the equilibrium potential of the considered redox reaction.

Here we choose a reference state based on the reference inflow condition $c_{\mathrm{ref}} = c^{\mathrm{in}}_{\mathrm{ox,ref}} = c^{\mathrm{in}}_{\mathrm{red,ref}}$ and assume for simplicity a symmetric reaction with $\alpha = 0.5$ in the rest of this work. In this work we adopt the convention that anodic currents and overpotentials have a positive sign.

Note that the local surface overpotential (measured just outside the double layer structure), $\eta_S = E - E_{\mathrm{eq}}$, still depends in general on the local electrolyte composition, since E_{eq} is a function of the local species concentrations: Rewriting the *practical* BV Eq. (7) in terms of the local

surface overpotential yields

$$\eta_S = E - E_{\text{eq}} = E - E_{\text{eq,ref}} + \frac{1}{f} \ln\left(\frac{c_{\text{red}}}{c_{\text{ox}}}\right) \tag{9}$$

with the current density

$$j = j_0 \left(e^{(1-\alpha) f \eta_S} - e^{-\alpha f \eta_S}\right), \tag{10}$$

where $j_0 = j_{0,\text{ref}} c_{\text{ox}}^{(1-\alpha)} c_{\text{ref}}^{\alpha}$ is the local exchange-current density.

Thanks to the assumption of negligible ohmic resistivity within the electrode and electrolyte, the electrode polarization E is spatially constant and thus also η_{ref}. Therefore, for a given reference concentration, overpotential, and symmetry coefficient, the electric current density j is a linear function of the species concentrations. As we show in detail further below, this property allows to recast the BV equation to a linear reaction law

$$j = -F k c_A \tag{11}$$

for the reaction

$$\text{A} \rightarrow \text{B}. \tag{12}$$

3.2 Characteristic Scales and Dimensionless Groups

In the following analysis it is convenient to cast all governing equations into their dimensionless equivalents. Such an approach has an advantage over dimensional formulation when working with a disparity of different scales as it reveals the dimensionless groups parameterizing the chemico-physical processes.

Let us introduce the nondimensional quantities

$$\bar{c} = \frac{c}{c^0}, \quad \bar{\mathbf{r}} = \frac{\mathbf{r}}{l^0}, \quad \bar{\mathbf{v}} = \frac{\mathbf{v}}{v^0}, \quad \bar{p} = \frac{p}{p^0}, \quad \bar{\eta} = \frac{\eta}{V^0}, \quad \bar{E} = \frac{E}{V^0}, \quad \bar{j} = \frac{j}{j^0} \tag{13}$$

defined with respect to the characteristic molar concentration c^0, length-scale l^0, velocity v^0, pressure p^0, current density j^0, and voltage V^0 defined by

$$c^0 = c_{\text{ref}}, \quad l^0 = l_x, \quad v^0 = \frac{l^0 p^0}{\mu}, \quad p^0 = l^0 |\nabla \langle p \rangle^{\beta}|, \quad j^0 = \frac{DFc^0}{l^0}, \quad V^0 = \frac{RT}{F} \tag{14}$$

where $c_{\text{ref}} = 1\,\text{M}$ is the characteristic species concentration, l_x denotes the size of a unit cell in the x-direction, $|\nabla \langle p \rangle^{\beta}|$ is the norm of the volume-averaged pressure gradient to be defined later, and V^0 is the thermal voltage.

One of the most important aspects of a dimensionless formulation is the identification of critical scaling parameters. Since for a given applied pressure difference the flow velocity is not known a priori, we define an alternative Reynolds number [2]

$$\mathrm{Re}_l^\star = \frac{\rho (l^0)^3}{\mu^2} |\nabla \langle p \rangle^\beta| \tag{15}$$

based on the applied pressure gradient, where ρ is the (constant) electrolyte density ($\mathrm{kg\,m^{-3}}$) and μ denotes the (constant) dynamic viscosity ($\mathrm{Pa\,s}$). Based on $\mathrm{Re}_l^\star$, we define the Péclet number

$$\mathrm{Pe}_l^\star = \frac{v^0 l^0}{D} = \mathrm{Re}_l^\star \mathrm{Sc}, \quad \text{with} \quad \mathrm{Sc} = \frac{\nu}{D}, \tag{16}$$

where Sc denotes the Schmidt number and $\nu = \mu/\rho$ is the kinematic viscosity of the electrolyte ($\mathrm{m^2\,s^{-1}}$). As we consider here aqueous electrolytes we set $\mathrm{Sc} = 1000$ in the remainder of this work.

The transport of the electroactive species i in the β-phase is then described by the diffusion-advection equation given in nondimensional form as

$$\mathrm{Pe}_l^\star \bar{\mathbf{v}} \cdot \bar{\nabla} \bar{c}_i = \bar{\nabla}^2 \bar{c}_i, \quad \bar{\mathbf{r}} \in \bar{V}_\beta. \tag{17}$$

The dimensionless scaling parameter controlling the importance of the electrochemical reaction with respect to diffusive transport is

$$\mathrm{Ki}_l = \frac{k l^0}{D}, \tag{18}$$

The nondimensional reactive boundary condition for the linear reaction law is then given by

$$-\bar{\nabla} \bar{c}_\mathrm{a} \cdot \mathbf{n}_{\beta\sigma} = -\mathrm{Ki}_l \bar{c}_\mathrm{a}, \quad \bar{\mathbf{r}} \in \bar{A}_{\beta\sigma}. \tag{19}$$

Similarly, to nondimensionalize the BV-type reaction Eq. (7) and the respective boundary condition into dimensionless form, we define the anodic and cathodic kinetic numbers as

$$\mathrm{Ki}_l^\mathrm{a} = \frac{kl}{D} a_\mathrm{a} = \mathrm{Ki}_l a_\mathrm{a}, \quad \mathrm{Ki}_l^\mathrm{c} = \frac{kl}{D} a_\mathrm{c} = \mathrm{Ki}_l a_\mathrm{c} \quad \text{with} \quad a_\mathrm{a} = e^{(1-\alpha) f \eta_\mathrm{ref}}, \quad a_\mathrm{c} = e^{-\alpha f \eta_\mathrm{ref}}, \tag{20}$$

so that the dimensionless form of the BV equation reads

$$\bar{j} = \mathrm{Ki}_l^a \bar{c}_\mathrm{red} - \mathrm{Ki}_l^c \bar{c}_\mathrm{ox}, \quad \bar{\mathbf{r}} \in A_{\beta\sigma} \tag{21}$$

with the corresponding reactive boundary conditions

$$-\bar{\nabla} \bar{c}_\mathrm{red} \cdot \mathbf{n}_{\beta\sigma} = \bar{j}, \quad -\bar{\nabla} \bar{c}_\mathrm{ox} \cdot \mathbf{n}_{\beta\sigma} = -\bar{j}, \quad \bar{\mathbf{r}} \in A_{\beta\sigma}. \tag{22}$$

To simplify the notation we will drop the *overline* symbol in the following to denote nondimensional quantities.

3.3 Upscaling the Transport Equations

In the VAM approach, the pore-scale transport equations are averaged over an REV (here corresponding to a unit-cell) to derive the governing macroscopic transport equation and effective transport parameters.

The *intrinsic averaging operator* for any field variable f defined over the electrolyte domain V_β reads [49]

$$\langle f \rangle^\beta = \frac{1}{\mathscr{V}_\beta} \int_{V_\beta} f \, dV \quad \text{with} \quad \mathscr{V}_\beta = \int_{V_\beta} 1 \, dV, \tag{23}$$

where $\mathscr{V}_\beta$ is the volume of the β-phase. The electrode porosity can be then expressed as $\varepsilon = \mathscr{V}_\beta / \mathscr{V}$, where $\mathscr{V}$ is the total unit-cell volume. Defining analogously the intrinsic averaging operator over the solid electrode domain V_σ allows to express the total volume as $\mathscr{V} = \mathscr{V}_\beta + \mathscr{V}_\sigma$.

Generally, any field f can be decomposed into its (intrinsic) average value and a remaining part $\tilde{f}$ indicating deviations from the averaged value as

$$f = \langle f \rangle^\beta + \tilde{f}. \tag{24}$$

Additionally, the *superficial averaging operator* is given by

$$\langle f \rangle = \frac{1}{\mathscr{V}} \int_{V_\beta} f \, dV, \tag{25}$$

so that the superficial average is related to the intrinsic average by $\langle f \rangle = \varepsilon \langle f \rangle^\beta$.

Similarly, we define the *interfacial surface average operator*

$$\langle f \rangle_{\beta\sigma} := \frac{1}{\mathscr{A}_{\beta\sigma}} \int_{A_{\beta\sigma}} f \, dA_{\beta\sigma} \quad \text{with} \quad \mathscr{A}_{\beta\sigma} = \int_{A_{\beta\sigma}} 1 \, dA_{\beta\sigma}, \tag{26}$$

where $A_{\beta\sigma}$ is the interfacial surface domain between the β and σ domains within a unit cell and $\mathscr{A}_{\beta\sigma}$ denotes the corresponding interfacial surface area.

Comprehensive derivations of the VAM are available in the literature (see e.g. [2, 43, 49]). Therefore, we will focus in the following on presenting the main results relevant for the current study.

3.3.1 Momentum Conservation

The electrolyte flow is governed by the incompressible Stokes equation, which can be written in nondimensional form as [2]

$$\nabla\langle p\rangle^{\beta}+\nabla\tilde{p}-\nabla^{2}\mathbf{v}=0,\quad \nabla\cdot\mathbf{v}=0,\quad \mathbf{r}\in V_{\beta}, \tag{27}$$

where the pressure field is decomposed as

$$p=\langle p\rangle^{\beta}+\tilde{p}. \tag{28}$$

The pressure deviation field $\tilde{p}$ satisfies the periodic boundary condition

$$\tilde{p}(\mathbf{r}+\mathbf{l}_i)=\tilde{p}(\mathbf{r}),\quad \text{with}\quad \mathbf{l}_i=\mathbf{e}^{(i)}l_i, \tag{29}$$

where $\mathbf{e}^{(i)}$ is the ith unit basis vector and l_i is the corresponding unit cell length. As a result, the volume-averaged dimensionless pressure gradient in Eq. (27), $\nabla\langle\tilde{p}\rangle^{\beta}$, is a unit vector (due to the selection of l_0 as the characteristic length) and its orientation dictates the direction of the electrolyte flow.

The electrolyte is assumed to have zero velocity at the fibre surfaces (no-slip condition) and the velocity field is periodic over the REV, that is

$$\mathbf{v}(\mathbf{r}+\mathbf{l}_i)=\mathbf{v}(\mathbf{r}). \tag{30}$$

Upscaling of the Stokes equation with the VAM yields the well-known Darcy law, see e.g. [48], which can be expressed in nondimensional form as

$$\mathbf{K}_l\cdot\nabla\langle p\rangle^{\beta}=-\langle\mathbf{v}\rangle, \tag{31}$$

where $\mathbf{K}_l$ is a symmetric and positive-definite permeability tensor, which is nondimensionalized with the characteristic scale $\mathbf{K}_l^0=(l^0)^2$.

3.3.2 First-order Heterogeneous Chemical Reaction

The application of the intrinsic volume averaging operator on the advection-diffusion equation and subsequent simplifications yields the macroscopic transport equation [43]

$$\varepsilon\mathrm{Pe}_l^{\star}\nabla\cdot\left(\langle c_i\rangle^{\beta}\langle\mathbf{v}\rangle^{\beta}\right)=\varepsilon\nabla\cdot\left[\left(\nabla\langle c_i\rangle^{\beta}+\frac{a_{l,v}}{\varepsilon}\langle\mathbf{n}_{\beta\sigma}\tilde{c}_i\rangle_{\beta\sigma}\right)-\mathrm{Pe}_l^{\star}\langle\tilde{c}\tilde{\mathbf{v}}\rangle^{\beta}\right]-a_{l,v}\mathrm{Ki}_l\left(\langle c_i\rangle^{\beta}+\langle\tilde{c}_i\rangle_{\beta\sigma}\right) \tag{32}$$

This transport equation is unclosed, since the deviation fields $\tilde{c},\tilde{\mathbf{v}}$ are not known at the macroscale.

To derive a closed-form macroscopic transport equation, a closure ansatz is used for the deviation fields, e.g., for the concentration fields the ansatz

$$\tilde{c}_i = \mathbf{f} \cdot \nabla \langle c_i \rangle^\beta + g \langle c_i \rangle^\beta \tag{33}$$

is inserted into the unclosed form of the transport equation, where $\mathbf{f}$ and g are unknown closure variables. As shown in [43], this results in the following periodic closure problems

$$\mathrm{Pe}_l^\star (\tilde{\mathbf{v}} + \mathbf{v} \cdot \nabla \mathbf{f}) = \nabla^2 \mathbf{f} + \mathrm{Ki}_l \langle \mathbf{f} \rangle_{\beta\sigma}, \quad \mathbf{r} \in V_\beta, \tag{34}$$

$$-\mathbf{n}_{\beta\sigma} \cdot \nabla \mathbf{f} = \mathrm{Ki}_l \mathbf{f} + \mathbf{n}_{\beta\sigma}, \quad \mathbf{r} \in A_{\beta\sigma}, \tag{35}$$

$$\mathbf{f}(\mathbf{r}) = \mathbf{f}(\mathbf{r} + \mathbf{l}_i) \quad \mathbf{r} \in V, \quad i = 1,2,3, \tag{36}$$

$$\langle \mathbf{f} \rangle^\beta = 0, \tag{37}$$

and

$$\mathrm{Pe}_l^\star \mathbf{v} \cdot \nabla g = \nabla^2 g + \mathrm{Ki}_l \left(\frac{a_{l,v}}{\varepsilon} + \langle g \rangle_{\beta\sigma} \right), \quad \mathbf{r} \in V_\beta, \tag{38}$$

$$-\mathbf{n}_{\beta\sigma} \cdot \nabla g = (g+1)\mathrm{Ki}_l, \quad \mathbf{r} \in A_{\beta\sigma}, \tag{39}$$

$$g(\mathbf{r}) = g(\mathbf{r} + \mathbf{l}_i) \quad \mathbf{r} \in V, \quad i = 1,2,3 \tag{40}$$

$$\langle g \rangle^\beta = 0. \tag{41}$$

The closed equation now reads

$$\varepsilon \mathrm{Pe}_l^\star \nabla \cdot \left(\langle c_\alpha \rangle^\beta \langle \mathbf{v} \rangle^\beta \right) = \nabla \cdot \left(\varepsilon \mathbf{D}^* \cdot \nabla \langle c_\alpha \rangle^\beta \right) - a_{l,v} \mathrm{Ki}^{\mathrm{eff}} \langle c_\alpha \rangle^\beta, \tag{42}$$

where $\mathbf{D}^*$ and $\mathrm{Ki}^{\mathrm{eff}}$ are the previously defined dimensionless total dispersion tensor and the effective kinetic number, respectively, both of which depend on $\mathbf{f}$ and g and are determined by resolving Eq. (37) and Eq. (41) according to

$$\mathbf{D}^* = \mathbf{I} + \frac{a_{l,v}}{\varepsilon} \langle \mathbf{n}_{\beta\sigma} \mathbf{f} \rangle_{\beta\sigma} - \mathrm{Pe}_l^\star \langle \mathbf{f} \tilde{\mathbf{v}} \rangle^\beta, \quad \mathrm{Ki}^{\mathrm{eff}} = \mathrm{Ki}_l \left(1 + \langle g \rangle_{\beta\sigma} \right), \tag{43}$$

where $\mathbf{I}$ is the identity matrix. Note that the total dispersion tensor combines the effect of the heterogeneous reaction (second right-hand side term) and hydrodynamic dispersion (third right-hand side term) on mass transport, so that in the case of no convective flow (i.e. $\mathrm{Pe}_l^\star = 0$), the dispersion tensor reduces to the effective diffusion tensor, since

$$\mathbf{D}^* = \mathbf{D}^{\mathrm{eff}} - \mathrm{Pe}_l^\star \langle \mathbf{f} \tilde{\mathbf{v}} \rangle^\beta. \tag{44}$$

3.3.3 Simplification of the Reactive Transport Equations

The transport equations for the electro-active species can be simplified by considering a change of variables from the individual species concentrations $(c_{\mathrm{ox}}, c_{\mathrm{red}})$ to the pair (c_T, c_{ox}), where c_T denotes the total species concentration $c_T = c_{\mathrm{ox}} + c_{\mathrm{red}}$, which satisfies the transport equation

$$\mathrm{Pe}_l^\star \mathbf{v} \cdot \nabla c_T = \nabla^2 c_T, \quad \mathbf{r} \in V_\beta, \tag{45}$$

$$-\nabla c_T \cdot \mathbf{n}_{\beta\sigma} = 0, \quad \mathbf{r} \in A_{\beta\sigma}. \tag{46}$$

Clearly, any constant function for the total species concentration c_T that satisfies the boundary conditions is a valid solution. This allows to reduce the transport problem to the equation

$$\mathrm{Pe}_l^\star \mathbf{v} \cdot \nabla c_{\mathrm{ox}} = \nabla^2 c_{\mathrm{ox}}, \quad \mathbf{r} \in V_\beta \tag{47}$$

$$-\nabla c_{\mathrm{ox}} \cdot \mathbf{n}_{\beta\sigma} = \mathrm{Ki}_l^{\mathrm{a}} \cdot (c_T - c_{\mathrm{ox}}) - \mathrm{Ki}_l^{\mathrm{c}} \cdot c_{\mathrm{ox}}, \quad \mathbf{r} \in A_{\beta\sigma}. \tag{48}$$

The boundary condition of Eq. (48) can be written equivalently as

$$-\nabla c_{\mathrm{ox}} \cdot \mathbf{n}_{\beta\sigma} = k_0' - k_1' c_{\mathrm{ox}}, \quad \mathbf{r} \in A_{\beta\sigma}, \tag{49}$$

where $k_0' = \mathrm{Ki}_l^{\mathrm{a}} c_{\mathrm{T}}$ and $k_1' = \mathrm{Ki}_l^{\mathrm{a}} + \mathrm{Ki}_l^{\mathrm{c}}$. Finally, using the variable transformation

$$c_{\mathrm{ox}} = c_{\mathrm{ox}}' + \frac{k_0'}{k_1'}, \quad c_T = c_T', \tag{50}$$

allows to write the transport equation with a linear reaction law as

$$\mathrm{Pe}_l^\star \mathbf{v} \cdot \nabla c_{\mathrm{ox}}' = \nabla^2 c_{\mathrm{ox}}', \quad \mathbf{x} \in V_\beta, \tag{51}$$

$$-\nabla c_{\mathrm{ox}}' \cdot \mathbf{n}_{\beta\sigma} = -k_1' c_{\mathrm{ox}}', \quad \mathbf{x} \in A_{\beta\sigma}. \tag{52}$$

This allows to reduce the problem of up-scaling the advection-diffusion equation coupled to a BV-type reaction law to the case of a linear reaction law.

The closed-form macroscopic transport equation immediately follows as

$$\mathrm{Pe}_l^\star \nabla \cdot (\varepsilon \langle \mathbf{v} \rangle^\beta \langle c_{\mathrm{ox}}' \rangle^\beta) = \nabla \cdot (\varepsilon \mathbf{D}^* \nabla \langle c_{\mathrm{ox}}' \rangle^\beta) - a_{l,v} k_1' \left(1 + \langle g \rangle_{\beta\sigma}\right) \langle c_{\mathrm{ox}}' \rangle^\beta, \tag{53}$$

which can be stated in terms of the species concentration variable c_{ox} as

$$\mathrm{Pe}_l^\star \nabla \cdot (\varepsilon \langle \mathbf{v} \rangle^\beta \langle c_{\mathrm{ox}} \rangle^\beta) = \nabla \cdot (\varepsilon \mathbf{D}^* \nabla \langle c_{\mathrm{ox}} \rangle^\beta) - a_{l,v} \mathrm{Ki}_{\mathrm{BV}}^{\mathrm{eff}} \left(\langle c_{\mathrm{ox}} \rangle^\beta - \langle c_{\mathrm{ox}}^{\mathrm{eq}} \rangle^\beta \right), \tag{54}$$

where we have introduced the effective kinetic number for the BV reaction at the interface

$$\mathrm{Ki}_{\mathrm{BV}}^{\mathrm{eff}} = k_1' \left(1 + \langle g \rangle_{\beta\sigma}\right) = \mathrm{Ki}_l \left(e^{-\alpha\eta_{\mathrm{ref}}} + e^{(1-\alpha)\eta_{\mathrm{ref}}}\right)\left(1 + \langle g \rangle_{\beta\sigma}\right) \tag{55}$$

and the averaged equilibrium concentration

$$\langle c_{\mathrm{ox}}^{\mathrm{eq}} \rangle^{\beta} = \frac{k_0'}{k_1'} = c_T \frac{1}{1 + e^{-\eta_{\mathrm{ref}}}}, \tag{56}$$

which is a function of the overpotential η_{ref}. Additionally, we can introduce the kinetic number

$$\mathrm{Ki}_l^{\mathrm{BV}} = \mathrm{Ki}_l \left(e^{-\alpha\eta_{\mathrm{ref}}} + e^{(1-\alpha)\eta_{\mathrm{ref}}}\right), \tag{57}$$

for the BV-type reaction, which encodes the dependency on the reaction constant and overpotential. This relation allows to predict the behaviour of the BV reaction from first-order.

3.3.4 Alternative Dimensionless Scaling Parameters

Using the previously defined scaling parameters we introduce the classical Reynolds and Péclet numbers

$$\mathrm{Re}_l = \frac{\rho l^0 |\langle \mathbf{v} \rangle|}{\mu} = |\langle \bar{\mathbf{v}} \rangle| \mathrm{Re}_l^\star, \quad \mathrm{Pe}_l = \frac{l^0 |\langle \mathbf{v} \rangle|}{D} = |\langle \bar{\mathbf{v}} \rangle| \mathrm{Pe}_l^\star \tag{58}$$

defined with respect to the superficial average flow velocity, where we again employ *overline* symbols to differentiate nondimensional from dimensional quantities.

To facilitate the analysis and comparison of different pore-scale structures we additionally introduce dimensionless scaling parameters defined with respect to the fibre diameter d, which is considered fixed in this study.

The corresponding Reynolds, Péclet, and kinetic numbers defined with respect to d are given by

$$\mathrm{Re}_d = \mathrm{Re}_l \bar{d}, \quad \mathrm{Pe}_d = \mathrm{Pe}_l \bar{d}, \quad \mathrm{Ki}_d = \mathrm{Ki}_l \bar{d}, \tag{59}$$

where $\bar{d} = d/l^0$ is the dimensionless fibre diameter. Other dimensionless quantities, such as the permeability tensor, are defined analogously, e.g., $\mathbf{K}_d = \mathbf{K}_l \bar{d}^{-2}$.

3.4 Direct Numerical Simulation

Complementary to the VAM approach, we perform direct numerical simulations (DNS) to validate the results of the diffusion-advection-reaction equation. For a given geometry of the periodic unit cell, we create an array of N cells along the X-axis, as depicted in the lower panel

of Fig. 3. Next, we resolve the pore-scale transport equations Eq. (27), together with Eq. (17) and Eq. (19) for the first-order reaction or Eq. (52) for the BV reaction.

At the macroscopic boundaries (e.g. the inlet to the porous electrode compartment) we usually know or can measure the concentration of species (e.g. electrolyte composition). Therefore, Eq. (17) is completed with a constant concentration Dirichlet boundary condition

At the macroscopic inlet boundary we prescribe a fixed electrolyte concentration and impose a standard no-diffusion-flux BC at the outlet, i.e., for species i we set

$$c_i = c_i^{\mathrm{in}}(\mathbf{r}), \quad \mathbf{r} \in A_{\beta\mathrm{e}}^{\mathrm{in}}, \quad -\nabla c_i \cdot \mathbf{n}_{\beta\mathrm{e}} = 0, \quad \mathbf{r} \in A_{\beta\mathrm{e}}^{\mathrm{out}}. \tag{60}$$

Lastly, we set the symmetry BC on the remaining upper and lower faces of the macroscopic domain according to

$$-\mathbf{n}_{\beta\mathrm{e}} \cdot (\mathrm{Pe}_l^{\star}\mathbf{v} - \nabla c_{\mathrm{i}}) = 0, \quad \mathbf{r} \in \{A_{\beta\mathrm{e}}^{\mathrm{up}}, A_{\beta\mathrm{e}}^{\mathrm{down}}\}. \tag{61}$$

3.5 Periodic Unit Cells

To study the impact of different PE microstructures (e.g., fibre alignment or porosity) on the effective transport properties, we generate synthetic periodic PE geometries in 2D and 3D, which are juxtaposed in the upper panel of Fig. 3 for different porosity values.

The 2D geometries include the simple cubic (SC) and hexagonal (H) geometries composed of fibres with disc (d) and square (s) cross-sections. The 3D geometries include the mono-fibre SC in cross-flow (cf) and parallel-flow (pf) arrangements, face-centred cubic (FCC) and body-centred cubic (BCC) geometries, all of which have disc cross-sections.

The SCs geometry is only used to validate the result with the available data in the literature. For all other studies, we employ the disc cross-section as the square is rather unlikely to correspond to an actual carbon fibre shape in the PE for FB applications.

PEs that are either composed of spherical particles with mean sphere diameter d or cylindrical filaments of diameter d, the specific surface area of the PE can be stated in analytical form as [38]

$$a_{d,v} = b(1-\varepsilon), \tag{62}$$

where $b = 6$ for spherical particles and $b = 4$ for cylindrical filaments [8] and $a_{d,v} = a_{l,v}\bar{d}$ is the dimensionless specific surface area scaled with the fibre diameter. In Fig. 4 we show the specific surface areas $a_{d,v}$ of the considered geometries, where $a_{d,v}$ coincides with Eq. 62 for the SCd, SCh, and SCpf geometries. However, for the FCC and BCC structures the specific surface area is reduced, which is due to the overlapping region of the fibres.

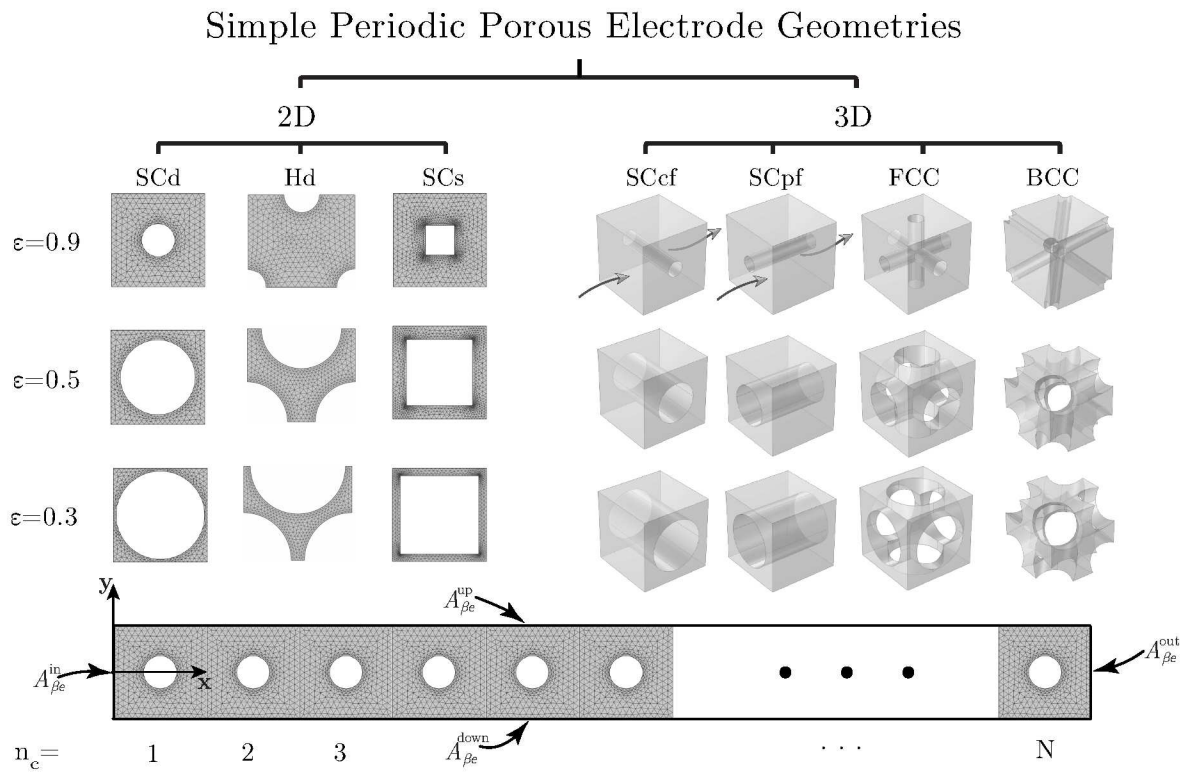

Figure 3: Upper panel: Simple periodic porous electrode geometries considered in this study in 2D and 3D: SC = simple cubic, H = hexagonal, FCC = face-centered cubic, BCC = body-centered cubic; d = fibres with disc cross-section, s = fibres with square cross-section (for literature study validation only), cf = cross-flow, pf = parallel flow. Lower panel: a PE geometry consisting of n SCd single cells, used in the DNS.

3.6 Characteristic Dimensionless Numbers in FB Systems

Electrochemistry deals with reaction constants k ranging over more than ten orders of magnitude. Single electron transfer reactions of $\mathcal{O}(k_0) = 10\ \mathrm{cm\,s^{-1}}$ without molecular structure reorganisation have been reported and can be regarded as relatively fast [3]. On the other hand, sluggish reactions with $\mathcal{O}(k) = 10^{-9}\ \mathrm{cm\,s^{-1}}$ are not uncommon in electrochemistry [3].

In most FB applications, k does not need to be extremely high, as the reaction rate is enhanced electrochemically by applying sufficiently large overpotentials [3]. However, k should also not be too low to prevent excessive activation polarisation and irreversibility of the redox reactions.

Based on given requirements of a FB system, such as high round-trip efficiency, cell voltage, specific surface area, electrolyte concentration, and conversion rate of electro-active species, Weber et al. [47] proposed a value $k = 10^{-5}\ \mathrm{cm\,s^{-1}}$ as the minimum rate constant for practical FB applications.

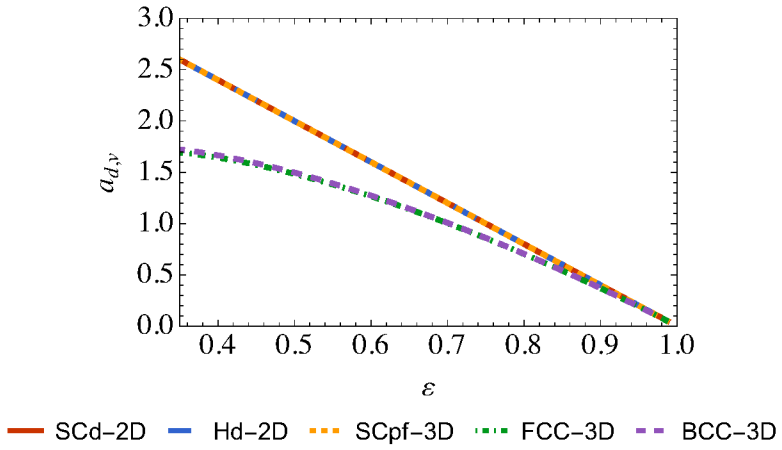

Figure 4: Specific surface areas of the considered geometries.

In Table 3 we show reported values of the reaction rate, diffusion coefficient and the dimensionless kinetic number Ki_d for a range of different FB systems. The listed values indicate that the reported redox-active organic molecules have a kinetic number in the range of $1 < \mathrm{Ki}_d < 10$, while e.g. the kinetic rates of the inorganic vanadium and bromine-based electrolytes are significantly smaller satisfying $\mathrm{Ki}_d < 0.1$.

FBs with relatively slow electrode kinetics such as VFBs require higher operating overpotentials in order to maintain high electrochemical reaction rates. From [1] (Fig. 2 therein) we estimate a typical activation loss in VFB system to be in the order of $350\,\mathrm{mV}$, which at $298.15\,\mathrm{K}$ yields the dimensionless overpotential of $\eta = 13.6$. For other systems in which the activation losses are lower due to rapid kinetics, the maximum expected η will also be lower.

To estimate the ranges of Péclet numbers Pe_d encountered in actual FB applications, we explored the available literature on (preferably experimental) FB studies. Milshtein [33] used a symmetric iron FB cell with carbon paper as the PE (25AA from SGL, assuming $\varepsilon = 0.75$). The cell operated at flow rates up to 10 $\mathrm{mL\,min^{-1}}$ (superficial velocity was estimated from the volumetric flow rate and electrode width and height). Milshtein et al. assumed a typical diffusion coefficient of ions in aqueous solution of $5 \cdot 10^{-6}\ \mathrm{cm^2\,s^{-1}}$, which yields the range of Péclet numbers $51 < \mathrm{Pe}_d < 1057$ for the characteristic fibre diameter $d = 1 \times 10^{-5}\,\mathrm{m}$ used in this work.

Finally, it is crucial to determine whether the electrolyte flow inside real FB can be modelled as creeping in order for Eq. (27) to hold. Xu et al. [51] studied flow through disordered and ordered 2D media with square pore cross-section using the LBM. By analysing e.g. the dependence of hydraulic permeability, $\mathbf{K}$, on Re_d (with the characteristic length d defined as the side length of the square fibre and the velocity being intrinsic), Xu et al. determined the critical Re_d at which $\mathbf{K}$ is not any more independent of Re_d, indicating the onset of the inertial regime. Based on the simulation results of Xu et al. (Figure 6 therein) we conclude that the critical Re_d

System	Species	k	D	Ki_d	Electrode	Comments	Source
Vanadium	VO^{2+}/VO_2^+	$1.35{\cdot}10^{-5}$	$2.26{\cdot}10^{-6}$	0.006	Planar glassy carbon	in 2 M H_2SO_4	[41]
Bromine-based	Br_2/Br^-	$5.80{\cdot}10^{-4}$	$1.60{\cdot}10^{-6}$	0.036	Vitreous carbon	Mean diffusion coefficient of bromine and bromide in water [22]	[47]
Aqueous organic, acidic	Anthraquinone-2,7-disulfonic acid (2,7 AQDS)	$7.20{\cdot}10^{-3}$	$3.80{\cdot}10^{-6}$	1.89	Glassy carbon	in 1 M H_2SO_4	[23]
Aqueous organic, alkaline	1,8-Dihydroxyanthraquinone (1,8-DHAQ)	$1.690{\cdot}10^{-2}$	$8.43{\cdot}10^{-6}$	6.01	Glassy carbon	in 1 M KOH	[7]
Aqueous organic, neutral	4-HO-TEMPO	$5.13{\cdot}10^{-2}$	$19.1{\cdot}10^{-6}$	2.00	Glassy carbon	in 1 M KCl	[30]
Hexaammineruthenium	$Ru(NH_3)_6^{3+}/Ru(NH_3)_6^{2+}$	0.8	$7.90{\cdot}10^{-6}$	101	Pt	in 1 M KCl	[6]
Ferro- and Ferricyanide	$Fe(CN)_6^{4-}/Fe(CN)_6^{3-}$	0.14	$6.30{\cdot}10^{-6}$	22.2	Pt	in 1 M NaCl	[6]

Table 3: Comparison of standard heterogeneous reaction rate constants, $k\,(\mathrm{cm\,s^{-1}})$ and diffusion coefficients, $D\,(\mathrm{cm^2\,s^{-1}})$ for a number of different redox active species commonly used in flow batteries.

depends significantly on both ε (critical Re_d increasing with decreasing ε) and the fibre alignment. However, the condition $\mathrm{Re}_d < 1$ in general ensures that inertial effects are insignificant, which for $\mathrm{Sc} = 1000$ is satisfied when $\mathrm{Pe}_d < 1000$, since $\mathrm{Pe}_d = \mathrm{Re}_d \mathrm{Sc}$.

Lastly, to estimate the practical ranges of ε for our simulations, we refer to the study by Zenyuk et al. [56] to conclude that the porosity of various carbon materials in FB applications normally spans between $\varepsilon = 0.6$ and $\varepsilon = 0.9$, depending strongly upon compression.

The above estimations serve as a basis for selecting ranges of the values of dimensionless numbers in parameter studies presented in the next section.

4 Results and Discussion

In this section we present numerical studies of the effective parameters determined by the VAM-based approach described previously. As we are interested in studying the effects of convection, diffusion and reaction on the macroscopic effective parameters, we focus here for simplicity on simple 1D flow problems over domains along the X-axis. This allows a reduction of the permeability, diffusion, and dispersion tensors to the scalar variables $K_{d,xx}$, D^{eff}_{xx}, and D^{*}_{xx}, respectively.

4.1 Model Verification

To verify our implemented VAM-based upscaling method we present the relevant effective parameters for a range of operating conditions against published results in Figure 5:

Fig. 5a displays the permeability coefficient $K_{\mathrm{d,xx}}$ over a large range of porosity values using the SCd structure, where the results of the current study coincide with the published results provided in [54] (Fig. 2a therein).

In Fig. 5b we show the total dispersion D^{*}_{xx} for the SCd geometry with $\varepsilon = 0.37$ over a range of particle Péclet numbers, which can be expressed as

$$\mathrm{Pe}_p = 6\frac{\mathrm{Pe}_d}{a_{d,v}}, \tag{63}$$

together with the predicted total dispersion in [13] (Fig. 12 therein). While in the limiting case of no convective flow $\mathrm{Pe}_p \to 0$ the dispersion coefficient converges to the effective diffusion, we observe a quadratic increase in D^{*}_{xx} for large Péclet numbers, which coincides with the Taylor-Aris dispersion relation, see e.g. [17].

In Fig. 5c we show the effective diffusion coefficient for the SCd and SCs structures with $\varepsilon = 0.8$ over a range of Kinetic numbers Ki_l, together with the results published in [43] (Figure 4a therein). In the limit of small reaction rates, $\mathrm{Ki}_l \to 0$, the effective diffusion converges to

a constant that depends only on the pore-scale geometry. On the other hand, in the limit of dominating reactions, $\mathrm{Ki}_l \to \infty$, the effective diffusion converges towards the molecular diffusion [43]. This behaviour can be explained by observing that only those species that are far from any reactive surface can diffuse between any two points without undergoing any chemical reaction. For the SCd geometry used here, species located far enough away from any electrode surface can diffuse along straight lines thanks to the geometrical arrangement of the periodic pore-scale structure, so that the respective effective diffusion along the x-direction corresponds to the molecular diffusion.

Finally, in Fig. 5d we show the result of a scaled effective kinetic number for the SCd geometry with $\varepsilon = 0.37$ over a range of kinetic numbers Ki_l, together with the results presented in [43]. The effective reaction rate can be observed to increase linearly for small kinetic numbers until a plateau is reached in the limit of large kinetic numbers for all values of Pe_l, due to diffusional transport limitations. While slight discrepancies at high kinetic rates $(\mathrm{Ki}_l > 100)$ and particle Péclet numbers $(\mathrm{Pe}_p > 100)$ can be observed, which may be caused by different numerical discretisation errors, the results of this study agree well with the published data.

Hamid and Smith [21] used a similar upscaling strategy to derive the effective mass transport in porous electrodes, for which they assumed facile electrochemical kinetics, which corresponds to the limiting case of large kinetic numbers.

The Sherwood number, defined as $\mathrm{Sh} = k_m d/D$, where k_m is the mass transfer coefficient $(\mathrm{m\,s^{-1}})$, is the ratio of the diffusion timescale d^2/D to the mass transport timescale d/k_m, indicating the importance of the mass transport (e.g., by convection and diffusion) with respect to diffusive transport. In the limiting case of large current densities we find that the Sherwood number is directly related to the effective kinetic number by $\mathrm{Sh} = \mathrm{Ki}_d^{\mathrm{eff}}$.

Fig. 6 shows the Sherwood number over a large range of Péclet numbers for the SCd-2D geometry and several porosity values, where we used a high kinetic number of $\mathrm{Ki}_d = 1000$ to approximate the limiting case studied in [21], illustrated as black symbols in the plot.

We conclude that the agreement with the reference data is excellent. Hamid and Smith noticed effects relevant for our further study: from the mass transport perspective alone, due to the redistribution of the diffusive flux at $1 < \mathrm{Pe}_d < 15$ and a dramatic increase of Sh, low porosity media are preferred in flow cells applications. However, low porosity media suffer from low hydraulic permeability, increasing pumping losses. In Section 4.3 we will reconsider these competing effects in an optimisation study.

4.1.1 Validation of the VAM against the DNS

To investigate the validity and accuracy of the VAM approach we compare the resulting macroscopic solution with fully-resolved DNS results. For this we consider the solution to the reactive

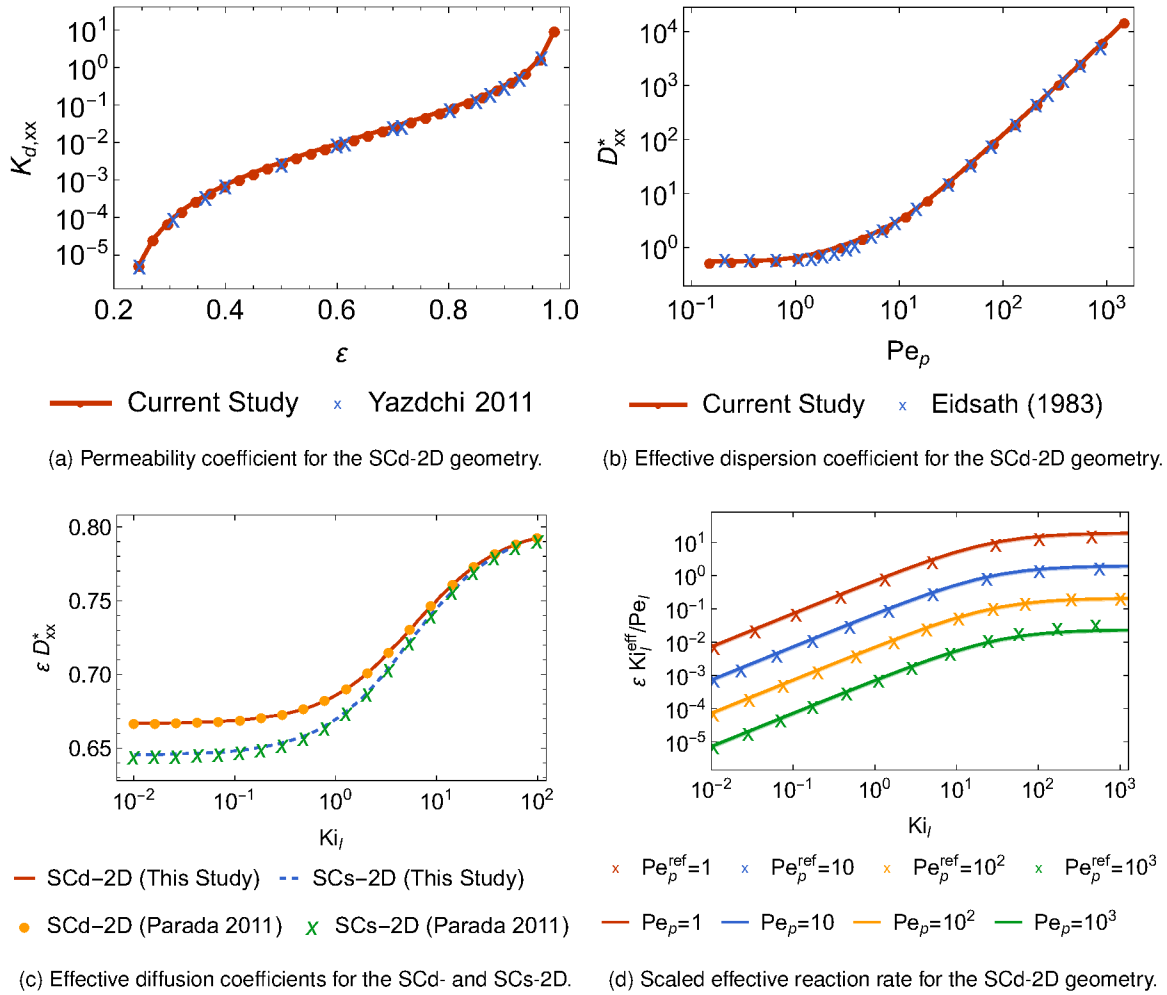

(a) Permeability coefficient for the SCd-2D geometry.

(b) Effective dispersion coefficient for the SCd-2D geometry.

(c) Effective diffusion coefficients for the SCd- and SCs-2D.

(d) Scaled effective reaction rate for the SCd-2D geometry.

Figure 5: Verification studies of the determined effective transport parameters.

mass transport problem over a one-dimensional domain shown in Fig. 2 and discussed in Section 3.4 in the context of the DNS approach.

For the considered transport problem we set the inflow concentration $c_{\mathrm{ox}}^{(\mathrm{in})} = 0.5$, the Péclet number $\mathrm{Pe}_l = 20.1$, and employ the BV-type reaction with kinetic number $\mathrm{Ki}_l = 1$ and overpotential $\eta_{\mathrm{ref}} = 0.5$, so that $\mathrm{Ki}_l^{\mathrm{BV}} \approx 2.06$. The pore-scale geometry is SCd-2D with porosity $\varepsilon = 0.9$.

In Fig. 7 we show the intrinsic average species concentration of c_{ox} of the upscaled macroscopic transport equation, together with the projected DNS solution $\langle c_{\mathrm{ox}}^{\mathrm{DNS}} \rangle_x^\beta$, which is evaluated by averaging the concentration of c_{ox} over the y-axis as

$$\langle c_{\mathrm{ox}}^{\mathrm{DNS}} \rangle_x^\beta = \frac{1}{\mathscr{V}_{\beta x}} \int_{V_{\beta x}} c_{\mathrm{ox}}^{\mathrm{DNS}}(x,y)\, dy \quad \text{with} \quad V_{\beta x}(x) = V_\beta \cap \{\mathbf{x} | \mathbf{x} \cdot \mathbf{e}^{(1)} = x\}, \quad \mathscr{V}_{\beta x} = |V_{\beta x}|. \tag{64}$$

Assuming a fibre diameter of $10\,\mu\mathrm{m}$, the corresponding dimensional unit cell length is $28\,\mu\mathrm{m}$,

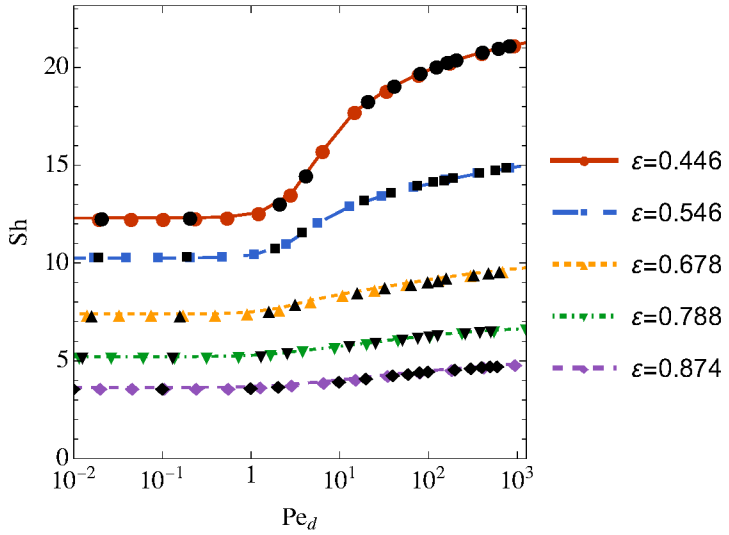

Figure 6: Dependency of the Sherwood number on the Péclet number for the SCd geometry with different porosity values, together with published results [21] (black symbols).

so that the overall domain lengths for $N = 10$ and $N = 30$ unit cells are $280\,\mu\text{m}$ and $841\,\mu\text{m}$, respectively. Clearly, this is still orders of magnitude smaller than typical macroscopic length scales in FB applications, for which the pore-scale concentration fluctuations of the DNS would be hardly resolvable.

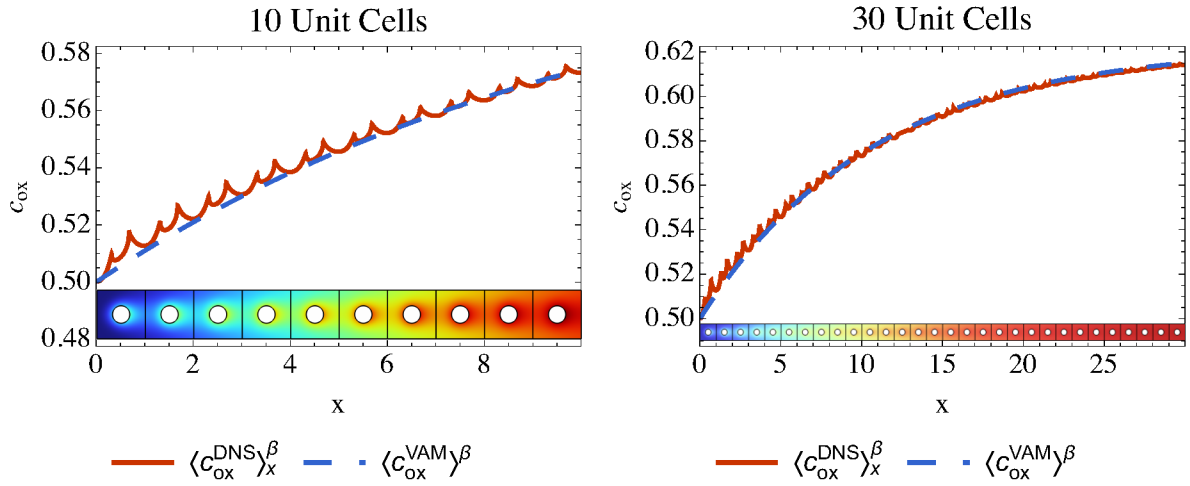

Figure 7: Intrinsic concentration averages of the VAM and DNS results over 10 and 30 unit cells.

Additionally, we verify the applicability of the VAM method for different flow velocities by varying Pe_l. Hence, we keep the same parameters and geometry (for $N = 30$) as described at the beginning of Section 4.1.1 and repeat the simulation for various Pe_l values as shown in Fig. 8.

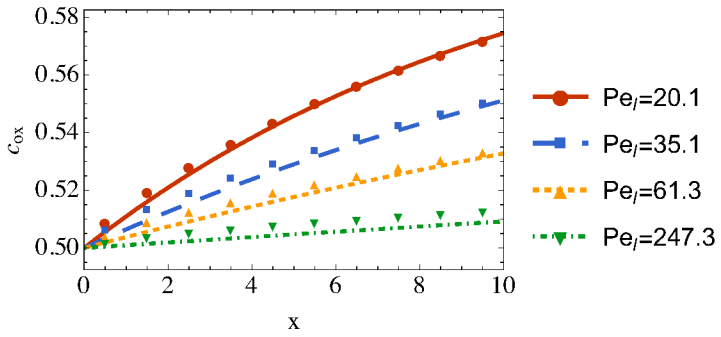

Figure 8: Comparison of VAM and DNS approaches for different Pe_l, where the symbols represent the cell-wise spatial averages of the DNS and the lines represent the VAM-based solution.

A comparison of the VAM solution (lines) with the cell-averaged DNS solution (symbols) reveals a general good agreement. However, the results reveal larger deviations of the VAM solution at higher Péclet numbers. This deviation is expected as the solution of high Péclet number flows through porous materials depends strongly on the macroscopic boundary condition. As the VAM assumes a local spatially periodic solution independent of macroscopic boundary conditions, it fails in representing such transport problems accurately close the macroscopic boundary.

4.2 Numerical Study of the Effective Parameters

In this section, we present additional numerical studies of the effective parameters over transport parameter ranges relevant for FB applications.

4.2.1 Permeability

Pressure drop is one of the key characteristics of FB systems as it is directly related to the parasitic losses due to the energy spent on pumping. Our model is capable of predicting the hydraulic permeability of the PE given the periodic unit cell geometry and porosity. In Fig. 9 we present the xx-component of the dimensionless hydraulic permeability tensor for all studied periodic geometries as a function of porosity.

The problem of predicting the permeability, for given meso-structures, has been discussed to a great extent in the literature [2, 32, 39, 40, 48, 53, 54], hence our modest contribution to this topic herein. In general, the largest relative difference in the permeability occurs at small porosities (e.g. below 0.5).

The evaluated permeabilities for the different structures fall in the same range of values determined by Kok et al. [27] for a carbon felt material, where permeability values in the range $K_{d,xx} \in [0.33, 0.58]$ were computed for estimated porosity values $\varepsilon \in [0.87, 0.93]$.

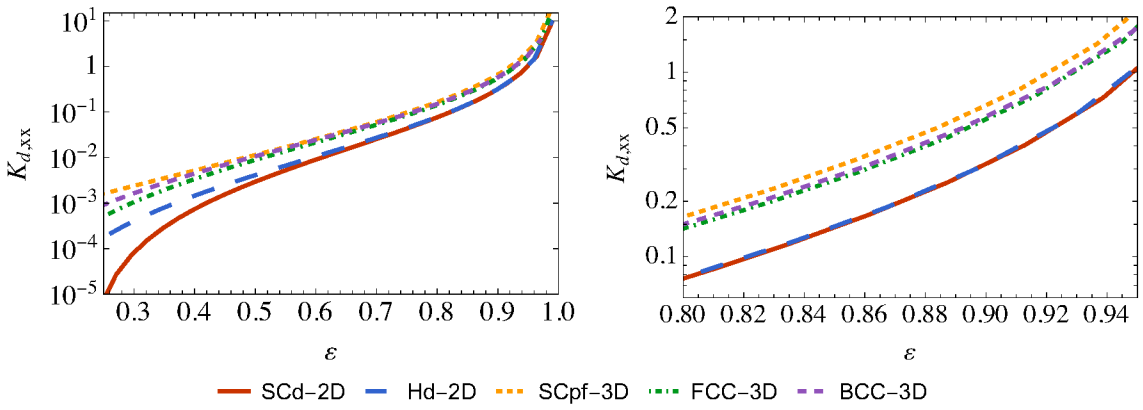

Figure 9: Dimensionless hydraulic permeability $K_{d,xx}$ of porous electrodes composed of different simple periodic structures as a function of porosity.

4.2.2 Effective Diffusion and Dispersion

The total dispersion tensor in PEs is affected by four factors: (1) the intrinsic molecular diffusion coefficient, (2) the meso-structure geometry, (3) the convective mass transport in the electrode, (4) as well as the reactions in the PE.

In Fig. 10a we show the dependency of the effective diffusion coefficient D_{xx}^{eff} on the kinetic number Ki_d for a passive diffusion transport $(\text{Pe}_d = 0)$ using different geometries with constant $\varepsilon = 0.9$. For the flow-aligned fibre structure SCpf we find that the chemical reaction has no effect on the diffusion as $D_{xx}^{\text{eff}} = 1$, since the flow-aligned structure allows particles to diffuse unhindered in straight paths along the x-direction, so that the effective diffusion rate equals the molecular diffusion. For all other investigated structures, we observe a reduced effective diffusion rate due to the blockage of the particles by the fibres, which leads to longer effective diffusion paths.

In Fig. 10b we show the total dispersion D_{xx}^{*} as a function of Pe_d for all considered geometries with constant $\varepsilon = 0.9$ and the kinetic number $\text{Ki}_d = 0.1$. We observe that the dispersion increases quadratically in Pe_d for all considered unit cells. Furthermore, we note a significant variation in the dispersion between the studied structures, where the flow-aligned structure shows the smallest dispersion, while the more complex FCC and BCC structures exhibit the highest dispersion.

4.2.3 Effectiveness Factor

The electrochemical reaction rate in a PE can be enhanced in three ways: (1) by increasing the rate constant, k (e.g. by increasing the temperature), (2) by intensifying mass transport by means of higher flow rates of electrolyte through the PE and (3) by increasing the overpoten-

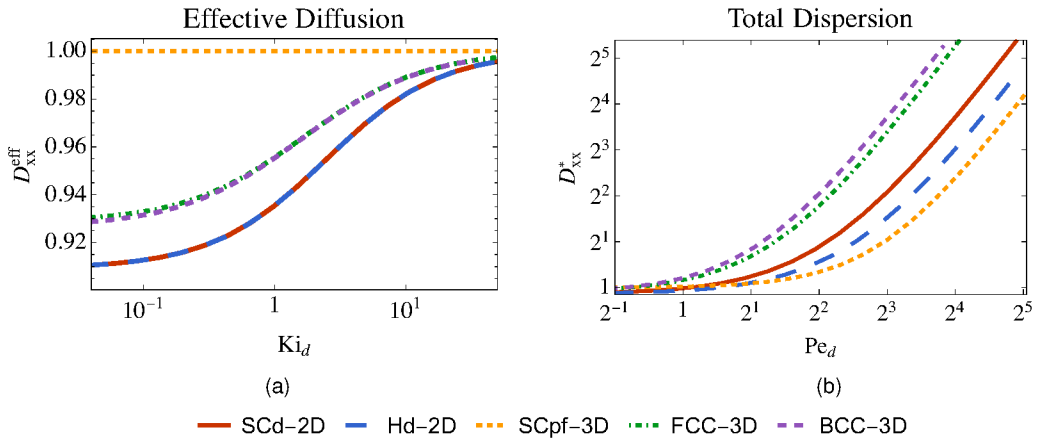

Figure 10: Total dispersion tensor (xx-component) as a function of (a) Ki_d and (b) Pe_d for different simple, periodic geometries (for other constant parameters cf. text)

tial at which the PE operates. To analyse the actual effectiveness of the electrode in terms of the electrochemical conversion impacted by all three factors, we define the dimensionless volumetric effectiveness factor, $\eta_v^{\mathrm{eff}} = a_{d,v}(1 + \langle g \rangle_{\beta\sigma})$.

The volumetric effectiveness factor η_v^{eff} is shown in Figure 11 (left) as a function of the kinetic number Ki_d for the passive diffusion scenario ($\mathrm{Pe}_d = 0$). In the limit of small kinetic numbers $\mathrm{Ki}_d \to 0$ we find $\langle g \rangle_{\beta\sigma} \to 0$, so that the volumetric effectiveness factor tends towards the specific surface area $a_{d,v}$. On the other hand, in the limit of large kinetic numbers, the volumetric effectiveness factor tends to zero, as the overall reaction rate becomes limited by the diffusion transport. We note a clustering of the results in two groups: The SCd, Hd, and SCpf structures show a very similar effectiveness factor and perform significantly better in comparison to the FCC and BCC structures. This difference can be explained by a lower specific surface area of the FCC and BCC structures. Figure 11 (right) displays the relative increase of η_v^{eff} due to convective flow over a range of Péclet numbers, where the kinetic number is held constant at $\mathrm{Ki}_d = 1$. While the effectiveness factor does not increase at higher Péclet numbers for the flow-aligned fibre structure SCpf, all other investigated structures display an increase in the effectiveness factor, which is most pronounced for the BCC structure.

4.3 Optimisation Study of the Pore-scale Structure

Let us apply the up-scaling methodology to the problem of determining optimal pore-scale geometries that maximize the overall efficiency of a porous electrode. For this we consider the simplified macroscopic one-dimensional porous electrode illustrated in Figure 12, where the electrolyte concentrations of the electroactive species at the inlet boundary is given by Dirichlet boundary conditions and simple natural Neumann boundary conditions are imposed on the

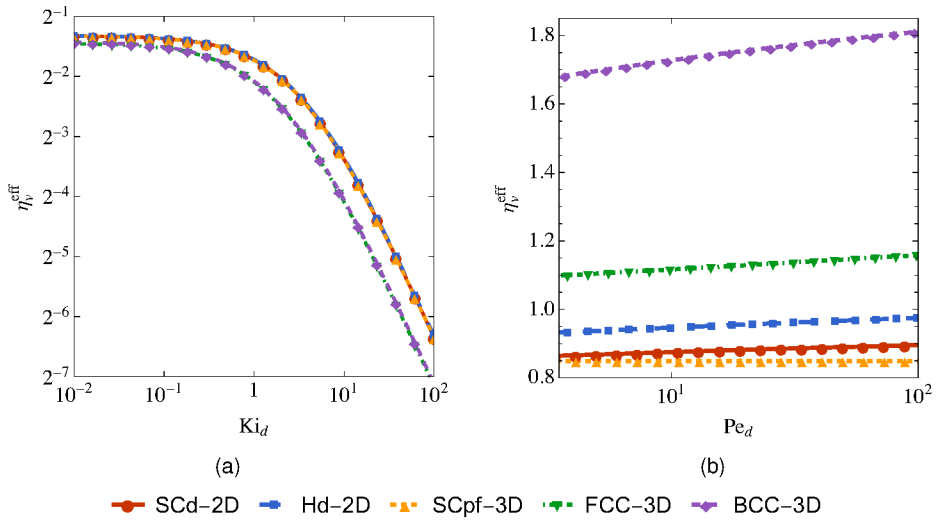

Figure 11: Electrode effectiveness factor as a function of Ki_d for passive diffusion (a) and with convection (b).

outlet boundary.

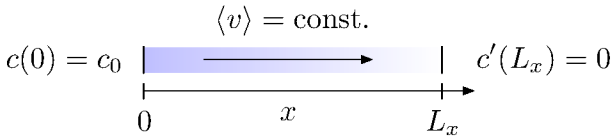

Figure 12: Illustration of macroscopic 1D porous electrode domain.

With the abbreviations $c \equiv \langle c \rangle^\beta$, $c^{\mathrm{eq}} \equiv \langle c^{\mathrm{eq}} \rangle^\beta$, the one-dimensional mass balance equation can be expressed as

$$\mathrm{Pe_M} c' = c'' - \mathrm{Ki_M^{eff}}(c - c^{\mathrm{eq}}), \quad c(0) = c_0, \quad c'(L_x) = 0, \tag{65}$$

where $\mathrm{Pe_M} = \mathrm{Pe}_d/(\varepsilon D^*)$ and $\mathrm{Ki_M^{eff}} = a_{d,v}\mathrm{Ki_d^{eff}}/(\varepsilon D^*)$ denote the Péclet and kinetic numbers scaled with respect to the effective macroscopic total dispersion and $a_{d,v}$.

For the above one-dimensional transport problem, the specific energy dissipation (defined as the dissipation of energy per mass of fluid flowing in the porous medium) can be stated in non-dimensional form by

$$\eta^{\mathrm{diss}} = \frac{\langle v \rangle^2}{\varepsilon K_{d,xx}}. \tag{66}$$

The analytical solution to Eq. (65) allows for a closed-form expression of the spatially averaged

reaction rate

$$\langle \mathrm{s} \rangle = \mathrm{Ki}_{\mathrm{d}}^{\mathrm{eff}} a_{d,v} \frac{1}{L_x} \int_0^{L_x} (c(x) - c^{\mathrm{eq}})\, dx. \tag{67}$$

In the following we set the macroscopic domain size to $L_x = 10^3$, which corresponds to a length of $1\,\mathrm{cm}$. Additionally, we consider the dimensionless inflow concentration of the reactant $c^{\mathrm{in}} = 0.5$, with an equilibrium concentration of $c^{\mathrm{eq}} = 1/(1+\exp(-\eta_{\mathrm{ref}}))$, where $\eta_{\mathrm{ref}} = -1$, and a kinetic reaction number of $\mathrm{Ki}_d = 1$.

Figure 13 displays the averaged reaction rate over a wide range of specific energy dissipation values for the considered pore-scale geometries at a fixed porosity values of $\varepsilon = 0.6$ (left) and $\varepsilon = 0.85$ (right). Ordering the structures from highest to lowest average reaction rate yields

$$\mathrm{SCpf} > \mathrm{Hd} \approx \mathrm{SCd} > \mathrm{FCC} > \mathrm{BCC} \tag{68}$$

for small specific energy dissipation values, whereas the ordering changes to

$$\mathrm{BCC} \approx \mathrm{SCpf} \approx \mathrm{FCC} > \mathrm{Hd} > \mathrm{SCd} \tag{69}$$

at high values of η^{diss}. These changes can be explained by the different permeability values of the structures: While the cross-flow aligned Hd and SCd structures allow for a high reaction rate compared to the FCC and BCC at low dissipation rates, their comparatively lower permeability leads at high flow velocities to increased energy dissipation rates, where both the FCC and BCC become favourable. Overall, the flow-aligned fibre structure SCpf shows very good performance.

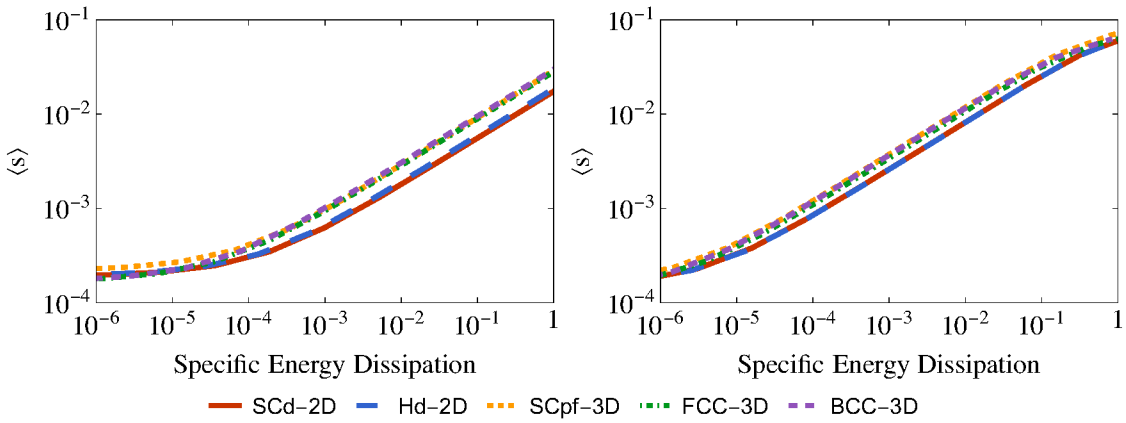

Figure 13: Average reaction rate over a range of specific energy dissipation values for the considered pore-scale structures with $\varepsilon = 0.6$ (left) and $\varepsilon = 0.85$ (right).

To investigate the impact of the porosity on the reaction rate, we show in Figure 14 the

performance of the flow-aligned structure SCpf for different porosity values. The results show that higher porosity values are favourable at lower specific energy dissipation values, whereas lower porosity values allow for an increased average reaction rate at higher dissipation rates thanks to their increased specific surface areas.

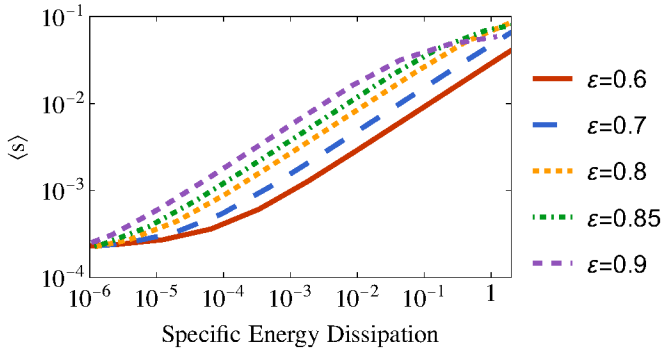

Figure 14: Average reaction rate over a range of specific energy dissipation values for the SCpf geometry with different porosity values.

4.4 Numerical Methods and Mesh Convergence Study

In the simulation studies carried out in this work we used the COMSOL Multiphysics software. For the mesh generation we employed an auto-generated mesh, whose mesh size and degrees of freedoms can be controlled by an auto mesh size parameter s, where $s = 1$ corresponds to the setting of the finest mesh setting, whereas larger values $(s = 2, 3, \ldots)$ correspond to further coarsened meshes. In Fig. 15 we show the relative error in the effective parameters D^* and $\mathrm{Ki}^{\mathrm{eff}}$ as a function of the auto mesh size parameter for the parameters $\varepsilon = 0.85, \mathrm{Pe}_d \approx 100, \mathrm{Ki}_d = 1$. The relative error is evaluated with respect to the most finely resolved mesh, which is here $s = 1$ for the 2D geometries and $s = 2$ for the 3D geometries, respectively. In this work we used $2 \leq s \leq 4$, depending on the problem and geometry so that the expected relative errors in the effective parameters are on the order of 1% for D^* and 0.1% for $\mathrm{Ki}^{\mathrm{eff}}$.

4.5 Surrogate model

In this work we have assumed the pore-scale geometry and transport conditions to be spatially homogeneous. However, the results presented here can also be applied to inhomogeneous materials or transport problems with spatially (or temporally) varying conditions, given that material property gradients and variations in operating conditions occur over macroscopic length scales much larger compared to a single unit cell, see [49].

When simulating transport problems through porous electrodes with variable material properties, such as spatially inhomogeneous porosity values in graded materials, there is a need for

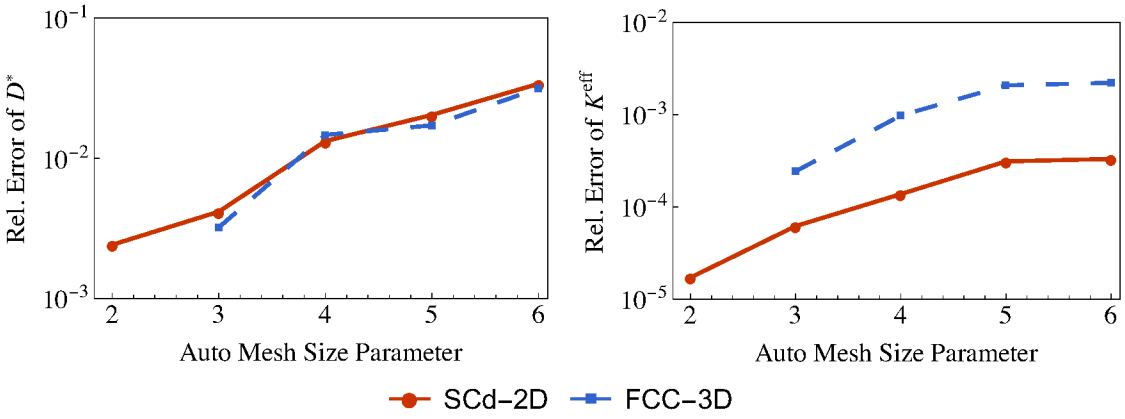

Figure 15: Relative discretisation error in the effective parameters.

repeated evaluation of the effective parameters. To avoid the necessity for numerous numerical solutions for the effective parameters when solving the macroscopic PDE we propose a two-step approach: (1) the effective parameters are solved for a set of parameter values that are sampled over a parameter space, whereby for each effective parameter a surrogate model is constructed using the evaluated effective transport coefficients at the sampled parameters, (2) which allows for an efficient online evaluation when solving the macroscopic transport equation.

Here we use the Kriging approach to provide a fast evaluation of the effective parameters. The Kriging estimator interpolates the given sample values and provides an estimation at the unsampled points based on a weighted average of the sampled values located in a neighbourhood, together with an estimate of the uncertainty. For each effective parameter $\mathrm{Ki}_d^{\mathrm{eff}}$, D_{xx}^* we generated a Kriging model using $N = 10^3$ samples over the parameter space $\mathrm{Pe}_d, \mathrm{Ki}_d, \varepsilon$.

5 Conclusions and Outlook

5.1 Summary

In this work we presented an application of the VAM to the mass transport in PEs with a BV type electrochemical reaction. Thanks to the simplifying assumptions it was possible to reduce the transport problem to the advection-diffusion equation with a linear reaction law using a suitable variable transformation.

We performed a dimensional analysis of the transport problem, which revealed the critical transport scaling parameters $\mathrm{Pe}_d, \mathrm{Ki}_d, \mathrm{Sc}$, where we fixed $\mathrm{Sc} = 1000$ in this study. Subsequently, we analysed the dependency of the effective transport parameters $K_{d,xx}$, $D_{d,xx}^*$, and $\mathrm{Ki}_d^{\mathrm{eff}}$ on the scaling parameters and the geometry, for which we studied two 2D and four 3D periodic structures parameterized by the porosity.

Validation studies for the predicted effective transport parameters showed very good agreement with published results. The numerical studies revealed the predicted permeability value for the investigated structures to be in a realistic range when compared to simulation results performed by Kok et al. [27]. The results presented in this work indicate that the ubiquitous usage of the analytical Bruggeman relation for the effective diffusion should be used with care when applied to FB applications as the Bruggeman relation neglects the effect of the heterogeneous reactions and convective flow on the effective total dispersion tensor.

In a next step we employed the evaluated effective parameters in a simple 1D transport problem in a macroscopic electrode, for which we determined the overall spatially averaged reaction rate for a given energy dissipation. This allowed to identify the optimal pore-scale structure for a given porosity value and conversely the optimal porosity value for a given pore-scale structure. The results indicate that the optimal structure depends on the operating conditions, where fibres aligned orthogonal to the convective flow direction are preferred at lower flow rates and fibres aligned parallel to the flow are preferred at higher flow rates. Additionally, the optimal porosity value was found to correlate inversely with the energy dissipation rate.

Finally, we constructed a surrogate model based on the Kriging method, which allows to efficiently evaluate the effective transport numbers for a given set of dimensionless pore-scale geometry and transport parameters. The surrogate model is especially useful in case of inhomogeneous materials with spatially or temporally varying properties, for which the effective parameters must be evaluated over a range of transport parameters. We will publish the model as open-source code on our GitHub account (*https://github.com/Isomorph-Electrochemical-Cells/RFB-SEMCS*), allowing the effective porous electrode parameters presented here to be easily included in cell models developed by other academic and industrial research groups.

6 Tables of Symbols and Acronyms

Symbols	Description	Unit
a_v	Specific (geometric) surface area	m^{-1}
A, $\mathscr{A}$	Surface domain, surface size ($\mathscr{A} = \lvert A \rvert$)	m^2
c	Molar concentration	$\mathrm{mol\,L}^{-1}$
d	Fibre diameter	m
D	Molecular diffusion coefficient	$\mathrm{m}^2\,\mathrm{s}^{-1}$
$\mathbf{D}^{\mathrm{eff}}$, $\mathbf{D}^*$	Effective diffusion and total dispersion tensors	m^2
E	Applied potential	V
f	Inverse thermal voltage ($f = F/(RT)$)	V^{-1}
F	Faraday constant	$\mathrm{C\,mol}^{-1}$
$\mathbf{f}, g$	Closure variables	–
$\mathbf{I}$	Identity matrix	–
j	Electric current density	$\mathrm{C\,m}^{-2}\,\mathrm{s}^{-1}$
k	Standard heterogeneous reaction rate constant	$\mathrm{m\,s}^{-1}$
k_0'	Zeroth-order reaction rate constant	$\mathrm{mol\,m}^{-2}\,\mathrm{s}^{-1}$
k_1'	First-order reaction rate constant	$\mathrm{m\,s}^{-1}$
$\mathrm{Ki}^{\mathrm{eff}}$	Effective kinetic number	$\mathrm{m\,s}^{-1}$
$\mathbf{K}$	Hydraulic permeability tensor	m^2
l	Mesoscopic characteristic length	m
L	Macroscopic characteristic length	m
$\mathbf{n}$	Normal vector	–
p	Pressure	Pa
$\mathbf{r}$	Position vector	m
r_0	Averaging radius	m
R	Universal gas constant	$\mathrm{J\,K}^{-1}\,\mathrm{mol}^{-1}$
T	Absolute temperature	K
$\mathbf{v}$	Flow velocity	$\mathrm{m\,s}^{-1}$
V, $\mathscr{V}$	Unit-cell domain, unit-cell volume ($\mathscr{V} = \lvert V \rvert$)	m^3
V^0	Thermal voltage ($V^0 = RT/F$)	V
x	Mole fraction	–

Greek symbols	Description	Unit
α	Symmetry factor in the Butler-Volmer model	–
η	Overpotential	V
ε	Electrode porosity	–
ρ	Electrolyte density	$\mathrm{kg\,m}^{-3}$
ν	Electrolyte kinematic viscosity	$\mathrm{m}^2\,\mathrm{s}^{-1}$
μ	Dynamic viscosity	$\mathrm{Pa\,s}$

Subscripts	Description
a	Refers to the anodic direction of the electrochemical reaction
c	Refers to the cathodic direction of the electrochemical reaction

d	Based on the fibre diameter (e.g., $a_{d,v}$)
e	Refers to the macroscale boundary
i	Refers to species i
l	Based on the unit cell length (e.g., $a_{l,v}$)
ox, red	Refers to oxidized or reduced species, respectively
T	Refers to the total concentration
β	Refers to the electrolyte phase (liquid)
σ	Refers to the porous electrode matrix phase (solid)
$\beta\sigma$	Refers to the interface between phases α and σ

Superscript	Description
0	Refers to characteristic scale
a	Refers to the anodic direction of the electrochemical reaction
c	Refers to the cathodic direction of the electrochemical reaction
eq	Refers to the electrochemical equilibrium condition
$\langle\cdot\rangle^{\beta}$	Refers to the intrinsic average over the void space
in, out	Refers to inlet and outlet boundaries

Dimensionless groups	Description
Re	Reynolds number (for definitions see text)
Sc	Schmidt number, $\mathrm{Sc} = \nu/D$
Pe	Péclet number (for definitions see text)
Pe_p	Particle Péclet number (for definitions see text)
$\mathrm{Ki}_l, \mathrm{Ki}_d$	Kinetic numbers $(\mathrm{Ki}_l = kl^0/D^0, \mathrm{Ki}_d = kd_f/D^0)$
$\mathrm{Ki}_l^{\mathrm{a}}$, $\mathrm{Ki}_l^{\mathrm{c}}$	Electrochemical anodic and cathodic kinetic numbers
Sh	Volumetric Sherwood number $(\mathrm{Sh} = a_v k_m l^0/D)$

References

[1] Doug Aaron et al. “Polarization Curve Analysis of All-Vanadium Redox Flow Batteries”. In: *J Appl Electrochem* 41.10 (Oct. 2011), pp. 1175–1182. ISSN: 0021-891X, 1572-8838. DOI: 10.1007/s10800-011-0335-7 (cit. on p. 20).

[2] Mehrez Agnaou et al. “Origin of the Inertial Deviation from Darcy’s Law: An Investigation from a Microscopic Flow Analysis on Two-Dimensional Model Structures”. In: *Phys. Rev. E* 96.4 (Oct. 9, 2017), p. 043105. ISSN: 2470-0045, 2470-0053. DOI: 10.1103/PhysRevE.96.043105 (cit. on pp. 7, 12–14, 26).

[3] Allen J. Bard and Larry R. Faulkner. *Electrochemical Methods: Fundamentals and Applications, 2nd Edition*. John Wiley & Sons, Dec. 4, 2000. 862 pp. ISBN: 978-1-118-31280-3. Google Books: hQocAAAAQBAJ (cit. on p. 19).

[4] Ilenia Battiato et al. “Theory and Applications of Macroscale Models in Porous Media”. In: *Transp Porous Med* 130.1 (Oct. 2019), pp. 5–76. ISSN: 0169-3913, 1573-1634. DOI: 10.1007/s11242-019-01282-2 (cit. on p. 6).

[5] Victor A. Beck et al. “Computational Design of Microarchitected Porous Electrodes for Redox Flow Batteries”. In: *Journal of Power Sources* 512 (Nov. 15, 2021), p. 230453. ISSN: 0378-7753. DOI: 10.1016/j.jpowsour.2021.230453 (cit. on p. 4).

[6] Carine Beriet and Derek Pletcher. “A Further Microelectrode Study of the Influence of Electrolyte Concentration on the Kinetics of Redox Couples”. In: *Journal of Electroanalytical Chemistry* 375.1 (Sept. 19, 1994), pp. 213–218. ISSN: 1572-6657. DOI: 10.1016/0022-0728(94)03359-5 (cit. on p. 21).

[7] Jianyu Cao et al. “A Highly Reversible Anthraquinone-Based Anolyte for Alkaline Aqueous Redox Flow Batteries”. In: *J. Power Sources* 386 (May 2018), pp. 40–46. ISSN: 03787753. DOI: 10.1016/j.jpowsour.2018.03.041 (cit. on p. 21).

[8] R. Carta et al. “Behaviour of a Carbon Felt Flow by Electrodes Part I: Mass Transfer Characteristics”. In: *J Appl Electrochem* 21.9 (Sept. 1991), pp. 793–798. ISSN: 0021-891X, 1572-8838. DOI: 10.1007/BF01402816 (cit. on p. 18).

[9] Barun Kumar Chakrabarti et al. “Modelling of Redox Flow Battery Electrode Processes at a Range of Length Scales: A Review”. In: *Sustainable Energy Fuels* 4.11 (2020), pp. 5433–5468. ISSN: 2398-4902. DOI: 10.1039/D0SE00667J (cit. on pp. 5, 6).

[10] Ding-Wen Chung et al. “Validity of the Bruggeman Relation for Porous Electrodes”. In: 21.7 (Oct. 2013), p. 074009. ISSN: 0965-0393. DOI: 10.1088/0965-0393/21/7/074009 (cit. on pp. 4, 5).

[11] Yohan Davit et al. “Homogenization via Formal Multiscale Asymptotics and Volume Averaging: How Do the Two Techniques Compare?” In: *Advances in Water Resources* 62 (Dec. 2013), pp. 178–206. ISSN: 03091708. DOI: 10.1016/j.advwatres.2013.09.006 (cit. on p. 6).

[12] Edmund J.F. Dickinson and Andrew J. Wain. “The Butler-Volmer Equation in Electrochemical Theory: Origins, Value, and Practical Application”. In: *Journal of Electroanalytical Chemistry* 872 (Sept. 2020), p. 114145. ISSN: 15726657. DOI: 10.1016/j.jelechem.2020.114145 (cit. on p. 10).

[13] A. Eidsath et al. “Dispersion in Pulsed Systems—III: Comparison between Theory and Experiments for Packed Beds”. In: *Chemical Engineering Science* 38.11 (Jan. 1, 1983), pp. 1803–1816. ISSN: 0009-2509. DOI: 10.1016/0009-2509(83)85037-4 (cit. on p. 22).

[14] Oladapo Christopher Esan et al. “Modeling and Simulation of Flow Batteries”. In: *Adv. Energy Mater.* (June 8, 2020), p. 2000758. ISSN: 1614-6832, 1614-6840. DOI: 10.1002/aenm.202000758 (cit. on p. 5).

[15] Antoni Forner-Cuenca and Fikile R. Brushett. “Engineering Porous Electrodes for Next-Generation Redox Flow Batteries: Recent Progress and Opportunities”. In: *Current Opinion in Electrochemistry* 18 (Dec. 2019), pp. 113–122. ISSN: 24519103. DOI: 10.1016/j.coelec.2019.11.002 (cit. on p. 4).

[16] Antoni Forner-Cuenca et al. “Exploring the Role of Electrode Microstructure on the Performance of Non-Aqueous Redox Flow Batteries”. In: *J. Electrochem. Soc.* 166.10 (2019), A2230–A2241. ISSN: 0013-4651, 1945-7111. DOI: 10.1149/2.0611910jes (cit. on p. 4).

[17] I. Frankel and H. Brenner. “On the Foundations of Generalized Taylor Dispersion Theory”. In: *J. Fluid Mech.* 204 (-1 July 1989), p. 97. ISSN: 0022-1120, 1469-7645. DOI: 10.1017/S0022112089001679 (cit. on p. 22).

[18] Andrea Gayon Lombardo et al. “A Pore Network Model of Porous Electrodes in Electrochemical Devices”. In: *Journal of Energy Storage* 24 (Aug. 2019), p. 100736. ISSN: 2352152X. DOI: 10.1016/j.est.2019.04.010 (cit. on p. 6).

[19] Fabrice Golfier et al. “Heat and Mass Transfer in Tubes: An Analysis Using the Method of Volume Averaging”. In: *JPM* 5.3 (2002). ISSN: 1091-028X, 1934-0508. DOI: 10.1615/JPorMedia.v5.i3.10 (cit. on p. 7).

[20] Jianwei Guo et al. “Dispersion in Porous Media with Heterogeneous Nonlinear Reactions”. In: *Transp Porous Med* 109.3 (Sept. 2015), pp. 541–570. ISSN: 0169-3913, 1573-1634. DOI: 10.1007/s11242-015-0535-4 (cit. on p. 7).

[21] Md Abdul Hamid and Kyle C. Smith. “Modeling the Transient Effects of Pore-Scale Convection and Redox Reactions in the Pseudo-Steady Limit”. In: *J. Electrochem. Soc.* 167.1 (2020), p. 013521. ISSN: 0013-4651, 1945-7111. DOI: 10.1149/2.0212001JES (cit. on pp. 23, 25).

[22] Brian Huskinson and Michael J Aziz. “Performance Model of a Regenerative Hydrogen Bromine Fuel Cell for Grid- Scale Energy Storage”. In: *Energy Sci. Technol.* (2013), p. 16 (cit. on p. 21).

[23] Brian Huskinson et al. “A Metal-Free Organic-Inorganic Aqueous Flow Battery”. In: *Nature* 505.7482 (Jan. 9, 2014), pp. 195–198. ISSN: 1476-4687. DOI: 10.1038/nature12909. pmid: 24402280 (cit. on p. 21).

[24] H. R. Jiang et al. “A Gradient Porous Electrode with Balanced Transport Properties and Active Surface Areas for Vanadium Redox Flow Batteries”. In: *Journal of Power Sources* 440 (Nov. 15, 2019), p. 227159. ISSN: 0378-7753. DOI: 10.1016/j.jpowsour.2019.227159 (cit. on p. 4).

[25] Xinyou Ke et al. “Redox Flow Batteries with Serpentine Flow Fields: Distributions of Electrolyte Flow Reactant Penetration into the Porous Carbon Electrodes and Effects on Performance”. In: *Journal of Power Sources* 384 (Apr. 30, 2018), pp. 295–302. ISSN: 0378-7753. DOI: 10.1016/j.jpowsour.2018.03.001 (cit. on p. 6).

[26] Dirk Kehrwald et al. “Local Tortuosity Inhomogeneities in a Lithium Battery Composite Electrode”. In: *J. Electrochem. Soc.* 158.12 (Nov. 4, 2011), A1393. ISSN: 1945-7111. DOI: 10.1149/2.079112jes (cit. on p. 5).

[27] Matthew D.R. Kok et al. “Mass Transfer in Fibrous Media with Varying Anisotropy for Flow Battery Electrodes: Direct Numerical Simulations with 3D X-ray Computed Tomography”. In: *Chemical Engineering Science* 196 (Mar. 2019), pp. 104–115. ISSN: 00092509. DOI: 10.1016/j.ces.2018.10.049 (cit. on pp. 26, 33).

[28] T.D. Le et al. “Multi-Scale Modeling of Diffusion and Electrochemical Reactions in Porous Micro-Electrodes”. In: *Chemical Engineering Science* 173 (Dec. 2017), pp. 153–167. ISSN: 00092509. DOI: 10.1016/j.ces.2017.07.039 (cit. on pp. 5, 7).

[29] Dongdong Li. “Phase Diagrams and Thermochemical Modeling of Salt Lake Brine Systems. I. LiCl+H2O System”. In: (2015), p. 12 (cit. on p. 5).

[30] Tianbiao Liu et al. “A Total Organic Aqueous Redox Flow Battery Employing a Low Cost and Sustainable Methyl Viologen Anolyte and 4-HO-TEMPO Catholyte”. In: *Adv. Energy Mater.* 6.3 (Feb. 2016), p. 1501449. ISSN: 16146832. DOI: 10.1002/aenm.201501449 (cit. on p. 21).

[31] Helen D. Lugo-Méndez et al. “Upscaling Diffusion and Nonlinear Reactive Mass Transport in Homogeneous Porous Media”. In: *Transp Porous Med* 107.3 (Apr. 2015), pp. 683–716. ISSN: 0169-3913, 1573-1634. DOI: 10.1007/s11242-015-0462-4 (cit. on p. 7).

[32] Nicola Luminari et al. “Effects of Porosity and Inertia on the Apparent Permeability Tensor in Fibrous Media”. In: *International Journal of Multiphase Flow* 106 (Sept. 2018), pp. 60–74. ISSN: 03019322. DOI: 10.1016/j.ijmultiphaseflow.2018.04.013 (cit. on p. 26).

[33] Jarrod D. Milshtein et al. “Quantifying Mass Transfer Rates in Redox Flow Batteries”. In: *J. Electrochem. Soc.* 164.11 (2017), E3265–E3275. ISSN: 0013-4651, 1945-7111. DOI: 10.1149/2.0201711jes (cit. on p. 20).

[34] John Newman and William Tiedemann. “Porous-Electrode Theory with Battery Applications”. In: *AIChE J.* 21.1 (Jan. 1, 1975), pp. 25–41. ISSN: 1547-5905. DOI: 10.1002/aic.690210103 (cit. on p. 5).

[35] Kyeongmin Oh et al. “Three-Dimensional, Transient, Nonisothermal Model of All-Vanadium Redox Flow Batteries”. In: *Energy* 81 (Mar. 2015), pp. 3–14. ISSN: 03605442. DOI: 10.1016/j.energy.2014.05.020 (cit. on p. 5).

[36] K. R. Rushton. *Groundwater Hydrology: Conceptual and Computational Models*. 1st edition. Hoboken, NJ: Wiley, Nov. 7, 2003. 430 pp. ISBN: 978-0-470-85004-6 (cit. on p. 7).

[37] Eduardo Sánchez-Díez et al. “Redox Flow Batteries: Status and Perspective towards Sustainable Stationary Energy Storage”. In: *Journal of Power Sources* 481 (Jan. 1, 2021), p. 228804. ISSN: 0378-7753. DOI: 10.1016/j.jpowsour.2020.228804 (cit. on p. 3).

[38] Ulf D. Schiller and Fang Wang. “Multiscale Simulation of Transport Phenomena in Porous Media: From Toy Models to Materials Models”. In: *MRS Commun.* 8.2 (June 2018), pp. 358–371. ISSN: 2159-6859, 2159-6867. DOI: 10.1557/mrc.2018.29 (cit. on pp. 6, 18).

[39] Raphael Schulz et al. “Beyond Kozeny–Carman: Predicting the Permeability in Porous Media”. In: *Transp Porous Med* 130.2 (Nov. 2019), pp. 487–512. ISSN: 0169-3913, 1573-1634. DOI: 10.1007/s11242-019-01321-y (cit. on p. 26).

[40] Naoki Takano et al. “Microstructure-Based Evaluation of the Influence of Woven Architecture on Permeability by Asymptotic Homogenization Theory”. In: *Composites Science and Technology* 62.10-11 (Aug. 2002), pp. 1347–1356. ISSN: 02663538. DOI: 10.1016/S0266-3538(02)00076-3 (cit. on p. 26).

[41] Tim Tichter et al. “Finite Heterogeneous Rate Constants for the Electrochemical Oxidation of VO2+ at Glassy Carbon Electrodes”. In: *Front. Energy Res.* 8 (2020), p. 155. ISSN: 2296-598X. DOI: 10.3389/fenrg.2020.00155 (cit. on p. 21).

[42] Bernhard Tjaden et al. “On the Origin and Application of the Bruggeman Correlation for Analysing Transport Phenomena in Electrochemical Systems”. In: *Current Opinion in Chemical Engineering* 12 (May 2016), pp. 44–51. ISSN: 22113398. DOI: 10.1016/j.coche.2016.02.006 (cit. on p. 5).

[43] F.J. Valdés-Parada et al. “On Diffusion, Dispersion and Reaction in Porous Media”. In: *Chemical Engineering Science* 66.10 (May 2011), pp. 2177–2190. ISSN: 00092509. DOI: 10.1016/j.ces.2011.02.016 (cit. on pp. 7, 13–15, 22, 23).

[44] Francisco J. Valdés-Parada et al. “Diffusion and Heterogeneous Reaction in Porous Media: The Macroscale Model Revisited”. In: *Int. J. Chem. React. Eng.* 15.6 (Dec. 20, 2017). ISSN: 1542-6580. DOI: 10.1515/ijcre-2017-0151 (cit. on p. 7).

[45] W. W. Wallender and D. Buyuktas. “Dispersion in Spatially Periodic Porous Media”. In: *Heat Mass Transf.* 40.3-4 (Feb. 1, 2004), pp. 261–270. ISSN: 0947-7411, 1432-1181. DOI: 10.1007/s00231-003-0441-0 (cit. on p. 7).

[46] Rui Wang et al. “Achieving Gradient-Pore-Oriented Graphite Felt for Vanadium Redox Flow Batteries: Meeting Improved Electrochemical Activity and Enhanced Mass Transport from Nano- to Micro-Scale”. In: *J. Mater. Chem. A* 7.18 (2019), pp. 10962–10970. ISSN: 2050-7488, 2050-7496. DOI: 10.1039/C9TA00807A (cit. on p. 4).

[47] Adam Z. Weber et al. “Redox Flow Batteries: A Review”. In: *J Appl Electrochem* 41.10 (Oct. 2011), pp. 1137–1164. ISSN: 0021-891X, 1572-8838. DOI: 10.1007/s10800-011-0348-2 (cit. on pp. 19, 21).

[48] Stephen Whitaker. “The Forchheimer Equation: A Theoretical Development”. In: *Transp Porous Med* 25.1 (Oct. 1, 1996), pp. 27–61. ISSN: 1573-1634. DOI: 10.1007/BF00141261 (cit. on pp. 14, 26).

[49] Stephen Whitaker. *The Method of Volume Averaging*. Red. by Jacob Bear. Vol. 13. Theory and Applications of Transport in Porous Media. Dordrecht: Springer Netherlands, 1999. ISBN: 978-90-481-5142-4 978-94-017-3389-2. DOI: 10.1007/978-94-017-3389-2 (cit. on pp. 7, 13, 31).

[50] Brian D. Wood. “The Role of Scaling Laws in Upscaling”. In: *Advances in Water Resources* 32.5 (May 2009), pp. 723–736. ISSN: 03091708. DOI: 10.1016/j.advwatres.2008.08.015 (cit. on p. 7).

[51] A. Xu et al. “Lattice Boltzmann Simulation of Mass Transfer Coefficients for Chemically Reactive Flows in Porous Media”. In: *J. Heat Transf.* 140.5 (May 1, 2018), p. 052601. ISSN: 0022-1481, 1528-8943. DOI: 10.1115/1.4038555 (cit. on p. 20).

[52] Q. Xu and T.S. Zhao. “Fundamental Models for Flow Batteries”. In: *Prog. Energy Combust. Sci.* 49 (Aug. 2015), pp. 40–58. ISSN: 03601285. DOI: 10.1016/j.pecs.2015.02.001 (cit. on p. 3).

[53] K. Yazdchi et al. “Micro–Macro Relations for Flow through Random Arrays of Cylinders”. In: *Composites Part A: Applied Science and Manufacturing* 43.11 (Nov. 2012), pp. 2007–2020. ISSN: 1359835X. DOI: 10.1016/j.compositesa.2012.07.020 (cit. on p. 26).

[54] K. Yazdchi et al. “Microstructural Effects on the Permeability of Periodic Fibrous Porous Media”. In: *International Journal of Multiphase Flow* 37.8 (Oct. 1, 2011), pp. 956–966. ISSN: 0301-9322. DOI: 10.1016/j.ijmultiphaseflow.2011.05.003 (cit. on pp. 22, 26).

[55] Xin You et al. “2-D Model of a H2/Br2 Flow Battery with Flow-Through Positive Electrode”. In: *J. Electrochem. Soc.* 163.3 (Jan. 1, 2016), A447–A457. ISSN: 0013-4651, 1945-7111. DOI: 10.1149/2.0361603jes (cit. on p. 5).

[56] Iryna V. Zenyuk et al. “Gas-Diffusion-Layer Structural Properties under Compression via X-ray Tomography”. In: *Journal of Power Sources* 328 (Oct. 2016), pp. 364–376. ISSN: 03787753. DOI: 10.1016/j.jpowsour.2016.08.020 (cit. on p. 22).

[57] B.W. Zhang et al. “A Two-Dimensional Model for the Design of Flow Fields in Vanadium Redox Flow Batteries”. In: *Int. J. Heat Mass Transf.* 135 (June 2019), pp. 460–469. ISSN: 00179310. DOI: 10.1016/j.ijheatmasstransfer.2019.02.008 (cit. on pp. 3, 6).